

GA-NIFS: Black hole and host galaxy properties of two $z \simeq 6.8$ quasars from the NIRSpec IFU

Madeline A. Marshall^{1,2} , Michele Perna³, Chris J. Willott¹, Roberto Maiolino^{4,5,6}, Jan Scholtz^{4,5}, Hannah Übler^{4,5}, Stefano Carniani⁷, Santiago Arribas³, Nora Lützgendorf⁸, Andrew J. Bunker⁹, Stephane Charlot¹⁰, Pierre Ferruit¹¹, Peter Jakobsen^{12,13}, Hans-Walter Rix¹⁴, Bruno Rodríguez Del Pino³, Torsten Böker⁸, Alex J. Cameron⁹, Giovanni Cresci¹⁵, Emma Curtis-Lake¹⁶, Gareth C. Jones⁹, Nimisha Kumari¹⁷, Pablo G. Pérez-González³, and Sophie L. Reed¹⁸

¹ National Research Council of Canada, Herzberg Astronomy & Astrophysics Research Centre, 5071 West Saanich Road, Victoria, BC V9E 2E7, Canada

e-mail: madeline_marshall@outlook.com

² ARC Centre of Excellence for All Sky Astrophysics in 3 Dimensions (ASTRO 3D), Stromlo, Australia

³ Centro de Astrobiología (CAB), CSIC-INTA, Ctra. de Ajalvir km 4, Torrejón de Ardoz 28850, Madrid, Spain

⁴ Kavli Institute for Cosmology, University of Cambridge, Madingley Road, Cambridge CB3 0HA, UK

⁵ Cavendish Laboratory – Astrophysics Group, University of Cambridge, 19 JJ Thomson Avenue, Cambridge CB3 0HE, UK

⁶ Department of Physics and Astronomy, University College London, Gower Street, London WC1E 6BT, UK

⁷ Scuola Normale Superiore, Piazza dei Cavalieri 7, 56126 Pisa, Italy

⁸ European Space Agency, c/o STScI, 3700 San Martin Drive, Baltimore, MD 21218, USA

⁹ Department of Physics, University of Oxford, Keble Road, Oxford OX1 3RH, UK

¹⁰ Sorbonne Université, CNRS, UMR 7095, Institut d'Astrophysique de Paris, 98 bis Bd Arago, 75014 Paris, France

¹¹ European Space Agency, ESAC, Villanueva de la Cañada 28692, Madrid, Spain

¹² Cosmic Dawn Center (DAWN), Copenhagen, Denmark

¹³ Niels Bohr Institute, University of Copenhagen, Jagtvej 128, 2200 Copenhagen, Denmark

¹⁴ Max Planck Institute for Astronomy, Königstuhl 17, 69117 Heidelberg, Germany

¹⁵ INAF – Osservatorio Astrofisico di Arcetri, Largo E. Fermi 5, 50127 Firenze, Italy

¹⁶ Centre for Astrophysics Research, Department of Physics, Astronomy and Mathematics, University of Hertfordshire, Hatfield AL10 9AB, UK

¹⁷ AURA for the European Space Agency, Space Telescope Science Institute, 3700 San Martin Drive, Baltimore, MD 21218, USA

¹⁸ Department of Astrophysical Sciences, Princeton University, 4 Ivy Lane, Princeton, NJ 08544, USA

Received 7 February 2023 / Accepted 26 August 2023

ABSTRACT

Aims. Integral field spectroscopy (IFS) with JWST NIRSpec will significantly improve our understanding of the first quasars, by providing spatially resolved, infrared spectroscopic capabilities that cover key rest-frame optical emission lines that have been previously unobservable.

Methods. Here we present our results from the first two $z > 6$ quasars observed as a part of the Galaxy Assembly with NIRSpec IFS (GA-NIFS) GTO programme, with DELS J0411–0907 at $z = 6.82$ and VDES J0020–3653 at $z = 6.86$.

Results. By observing the $H\beta$, [O III] $\lambda\lambda 4959, 5007$, and $H\alpha$ emission lines in these high- z quasars for the first time, we measured accurate black hole masses, $M_{\text{BH}} = 1.85^{+2}_{-0.8} \times 10^9 M_{\odot}$ and $2.9^{+3.5}_{-1.3} \times 10^9 M_{\odot}$, corresponding to Eddington ratios of $\lambda_{\text{Edd}} = 0.8^{+0.7}_{-0.4}$ and $0.4^{+0.3}_{-0.2}$ for DELS J0411–0907 and VDES J0020–3653, respectively. These provide a key comparison for existing estimates from the more uncertain Mg II line. We performed quasar–host decomposition using models of the quasars' broad lines to measure the underlying host galaxies. We also discovered multiple emission line regions surrounding each of the host galaxies, which are likely companion galaxies undergoing mergers with these hosts. We measured the star formation rates, excitation mechanisms, and dynamical masses of the hosts and companions, measuring the $M_{\text{BH}}/M_{\text{dyn}}$ ratios at high z using these estimators for the first time. DELS J0411–0907 and VDES J0020–3653 both lie above the local black hole–host mass relation, and are consistent with the existing observations of $z \geq 6$ quasar host galaxies with ALMA. We detected ionised outflows in [O III] $\lambda\lambda 4959, 5007$ and $H\beta$ from both quasars, with mass outflow rates of 58^{+44}_{-37} and $525^{+75}_{-92} M_{\odot} \text{ yr}^{-1}$ for DELS J0411–0907 and VDES J0020–3653, much larger than their host star formation rates of <33 and $<54 M_{\odot} \text{ yr}^{-1}$, respectively.

Conclusions. This work highlights the exceptional capabilities of the JWST NIRSpec IFU for observing quasars in the early Universe.

Key words. quasars: supermassive black holes – quasars: emission lines – galaxies: high-redshift – galaxies: interactions – galaxies: active – ISM: jets and outflows

1. Introduction

Observational surveys over the last two decades have revealed several hundreds of high- z quasars ($z \gtrsim 6$; e.g. Fan et al. 2000,

2001, 2003; Willott et al. 2009, 2010; Kashikawa et al. 2015; Bañados et al. 2016, 2018; Banados et al. 2022; Matsuoka et al. 2018; Wang et al. 2019; Yang et al. 2023a), less than a billion years into the Universe's history. The black holes powering

these quasars have been measured to be as massive as $\sim 10^{10} M_{\odot}$ (Wu et al. 2015), raising questions about the nature of the first black hole seeds and their extreme growth mechanisms. Theories to explain the growth of these first quasars generally require massive black hole seeds, sustained accretion at the Eddington limit, or phases of accretion at super-Eddington rates (e.g. Volonteri & Rees 2005; Volonteri et al. 2015; Sijacki et al. 2009). Some quasars have indeed been measured to have accretion rates above the Eddington limit (e.g. Bañados et al. 2018; Pons et al. 2019; Farina et al. 2022); although, when considering the uncertain black hole mass measurements and a large scatter in the adopted scaling relations, Farina et al. (2022) found no clear evidence for a significant population of super-Eddington high- z quasars. Thus accurate measurements of the black hole mass and accretion rate for high- z quasars provide vital constraints for these theories.

Current high- z quasar black hole mass measurements rely on calibrations that can be quite uncertain. The $H\alpha$ and $H\beta$ lines are generally considered the most reliable single-epoch indicators of black hole mass, as they are used in many reverberation mapping studies (e.g. Wandel et al. 1999; Kaspi et al. 2000). However, these reverberation mapping studies are performed for low- z , low-luminosity active galactic nuclei (AGN). At higher z , and for luminous quasars, extrapolations are required, and so at high z even these best estimates are uncertain. More critically, for high- z quasars these lines are redshifted into infrared wavelengths $> 2.5 \mu\text{m}$, beyond the range observable from the ground (for sources at $z \gtrsim 4$ for $H\beta$ and $z \gtrsim 3$ for $H\alpha$). Thus black hole mass measurements for high- z quasars instead have typically relied on the Mg II and C IV lines. Reverberation mapping studies based on Mg II and C IV are more uncertain (e.g. Trevese et al. 2014; Kaspi et al. 2021), and the resulting scaling relations required to obtain single-epoch black hole mass estimates are affected by luminosity-dependent biases and provide highly uncertain mass measurements, for example due to significant blueshifts caused by outflows (e.g. Shen et al. 2008; Shen & Kelly 2012; Peterson 2009; Coatman et al. 2016; Farina et al. 2022, and references therein). With the *James Webb* Space Telescope (JWST; Gardner et al. 2006, 2023; McElwain et al. 2023) and the Near-Infrared Spectrograph (NIRSpec; Jakobsen et al. 2022; Böker et al. 2023), $H\beta$ is now observable up to $z = 9.8$, and $H\alpha$ up to $z = 7.0$ – and beyond with the Mid-Infrared Instrument (MIRI) –, allowing us to more accurately measure the black hole masses and Eddington ratios of high- z quasars with the same estimator at all redshifts (e.g. Eilers et al. 2022; Yang et al. 2023b). This will improve our understanding of the first black holes and their growth rates by determining whether these black holes are truly so massive, and whether they are accreting above the Eddington limit.

Significant questions also exist surrounding the nature of the galaxies in which these quasars reside. These hosts can be measured in the sub-millimetre, tracing their cold gas and dust, which reveals a varying population of objects with a wide range of dynamical masses (10^{10} – $10^{11} M_{\odot}$), dust masses (10^7 – $10^9 M_{\odot}$) and sizes (< 1 – 5 kpc), and star formation rates (SFRs, 10 – $2700 M_{\odot} \text{ yr}^{-1}$; e.g. Bertoldi et al. 2003; Walter et al. 2003, 2004, 2022; Riechers et al. 2007; Wang et al. 2010, 2011; Venemans et al. 2015, 2017; Willott et al. 2017; Trakhtenbrot et al. 2017; Izumi et al. 2018; Neeleman et al. 2021). However, their host galaxies have not been observed in the rest-frame UV/optical even with the resolution of the *Hubble* Space Telescope (HST; Mechtley et al. 2012; Decarli et al. 2012; McGreer et al. 2014; Marshall et al. 2020), due to the intense emission from the quasar concealing the small, fainter

galaxy underneath (e.g. Schmidt 1963; McLeod & Rieke 1994; Dunlop et al. 2003; Hutchings 2003).

The JWST not only allows us to access the near-infrared spectral range with unprecedented sensitivity, but also provides high angular resolution and a stable point-spread function (PSF). With these improvements over HST, simulations predict that the host galaxies of these high- z quasars will be detectable for the first time (Marshall et al. 2021), and indeed the first signs of host emission have been detected with the Near-Infrared Camera (NIRCam; Ding et al. 2023). Thus JWST and the NIRSpec Integral Field Unit (IFU; Böker et al. 2022) will permit the characterisation of the spatially resolved spectral properties of the hosts, measuring their stellar properties, interstellar medium (ISM) structure and kinematics, excitation mechanisms, and stellar-based SFRs. This will significantly advance our understanding of quasars, their host galaxies, and the rapid growth of early supermassive black holes.

Based on JWST and NIRSpec IFU observations, in this paper we use the standard $H\alpha$ and $H\beta$ single-epoch black hole mass estimators to derive accurate black hole mass measurements for two $z > 6$ quasars, DELS J0411–0907 and VDES J0020–3653. DELS J0411–0907 (VHS J0411–0907) at $z = 6.82$ was discovered independently by Pons et al. (2019) and Wang et al. (2019). DELS J0411–0907 is the most distant of the Pan-STARRS quasars, and is the brightest quasar in the J band above $z = 6.7$ (Pons et al. 2019). With a relatively low Mg II black hole mass of $(6.13 \pm 0.51) \times 10^8 M_{\odot}$, and a bolometric luminosity of $(1.89 \pm 0.07) \times 10^{47} \text{ erg s}^{-1}$, Pons et al. (2019) measured an Eddington ratio of 2.37 ± 0.22 , implying that this quasar could be a highly super-Eddington quasar undergoing extreme accretion. The quasar VDES J0020–3653 at $z = 6.86$ was discovered by Reed et al. (2019). VDES J0020–3653 has a larger Mg II black hole mass than DELS J0411–0907, measured as $(16.7 \pm 3.2) \times 10^8 M_{\odot}$ by Reed et al. (2019), and re-derived as $25.1 \times 10^8 M_{\odot}$ by Farina et al. (2022) using the Shen et al. (2011) Mg II–black hole mass relation. With a bolometric luminosity of $L_{\text{Bol}} = (1.35 \pm 0.03) \times 10^{47} \text{ erg s}^{-1}$, these correspond to Eddington ratios of 0.62 ± 0.12 and 0.43 , respectively, suggesting that this quasar is powered by a larger supermassive black hole with less extreme accretion than DELS J0411–0907. However, these black hole mass and accretion measurements are based on the Mg II line; robust $H\alpha$ and $H\beta$ mass estimates will better constrain the accretion of these quasars.

This paper is outlined as follows. In Sect. 2 we describe the JWST NIRSpec observations, and our data reduction and analysis techniques. In Sect. 3 we present our results, with the black hole properties in Sect. 3.1, the host galaxy properties in Sect. 3.2, and the outflow properties in Sect. 3.3. We present a discussion in Sect. 4, before concluding with a summary of our findings in Sect. 5. Throughout this work we adopt the WMAP9 cosmology (Hinshaw et al. 2013) as included in ASTROPY (Astropy Collaboration 2013), with $H_0 = 69.32 \text{ km}/(\text{Mpc s})$, $\Omega_m = 0.2865$, and $\Omega_{\Lambda} = 0.7134$.

2. Data, reduction, and analysis

2.1. Observations

DELS J0411–0907 and VDES J0020–3653 were observed as part of the Galaxy Assembly with NIRSpec Integral Field Spectroscopy (GA-NIFS) Guaranteed Time Observations (GTO) programme, contained within programme #1222 (PI: Willott). This work focuses on the observations of these two quasars with the NIRSpec IFU (Böker et al. 2022), which provides spatially

resolved imaging spectroscopy over a $3'' \times 3''$ field of view with $0.1'' \times 0.1''$ spatial elements. The IFU observations were taken with a grating/filter pair of *G395H/F290LP*. This results in a spectral cube with spectral resolution $R \sim 2700$ over the wavelength range $2.87\text{--}5.27\ \mu\text{m}$. The observations were taken with a NRSIRS2 readout pattern with 25 groups, using a 6-point medium cycling dither pattern, resulting in a total exposure time of 11 029 s. We constrained the complete position angle (PA) window available for observing these targets with JWST to a more limited PA range, to minimise the leakage of light through the micro-shutter assembly (MSA) from bright sources. Additionally, these quasars have been observed with NIRSpec fixed-slit spectroscopy at shorter wavelengths (with *G140H/F070LP*, *G235H/F170LP*), which will be analysed in a separate paper.

DELS J0411–0907 was observed on Oct. 1, 2022, at a PA of 61.893° . VDES J0020–3653 was observed on Oct. 16, 2022, at a PA of 160.169° . Unfortunately, only three out of the six planned dithers were observed due to a spacecraft guiding failure. The final three dithers were observed on Nov. 17, 2022, at a position angle of 188.177° . With half of the VDES J0020–3653 observations observed at a different PA, combining these exposures and their subsequent data analysis was more challenging than the DELS J0411–0907 observations. Due to an error in the reference files of the pipeline (see Perna et al. 2023, for details), we performed a bona fide astrometric registration matching the peak pixel locations of the $H\alpha$ BLR collapsed images. We applied a constant offset in RA and Dec to the pipeline Stage 1 products of the second set of observations, which allowed the pipeline to correctly combine all six dithers in a final data cube.

Due to an uncertainty in the specified astrometry of our observations, we assumed that the quasar was centred on the known positions from the literature: 04 h 11 m 28.63 s, $-09\text{d } 07\text{m } 49.8\text{ s}$ for DELS J0411–0907 (Wang et al. 2019) and 00 h 20 m 31.472 s, $-36\text{d } 53\text{m } 41.82\text{ s}$ for VDES J0020–3653 (Reed et al. 2019). These were the targeted positions for our IFU observations, which have been found to have a typical pointing accuracy of $\sim 0.1''$ compared to the requested pointing (Rigby et al. 2022).

2.2. Data reduction

The data reduction was carried out with the JWST calibration pipeline version 1.8.2 (Bushouse et al. 2022), using the context file `JWST_1023.PMAP`. All of the individual raw images were first processed for detector-level corrections using the `DETECTORPIPELINE` module of the pipeline (Stage 1 hereinafter). The individual products (count-rate images) were then calibrated through `CALWEBB_SPEC2` (Stage 2 hereinafter), where WCS-calibration, flat-fielding, and the flux-calibrations are applied to convert the data from units of count rate to flux density. The individual Stage 2 images were then re-sampled and co-added onto a final data cube through the `CALWEBB_SPEC3` processing (Stage 3 hereinafter). A number of additional steps and corrections in the pipeline code have been applied to improve the data reduction quality. In particular,

- The individual count-rate frames were further processed at the end of Stage 1, to correct for a different zero-level in the dithered frames. For each image, we therefore subtracted the median value, computed considering the entire image, to get a base-level consistent with zero counts per second.

- We further processed these count-rates to subtract the $1/f$ noise (Kashino et al. 2022). This correlated vertical noise is modelled in each column (i.e. along the spatial axis) with a low-order polynomial function, after removing all bright pixels

(e.g. associated with the observed target) with a sigma-clipping. The modelled $1/f$ noise was then subtracted before proceeding with the Stage 2 of the pipeline.

- The `OUTLIER_DETECTION` step of the third and last step of the pipeline is required to identify and flag all remaining cosmic-rays and other artefacts that result in a significant number of spikes in the reduced data. In pipeline version 1.8.2, this step tends to identify too many false positives that compromises the data quality significantly. We therefore implemented a modified version of the `LACOSMIC` algorithm (van Dokkum 2001) in the JWST pipeline, which was applied at the end of Stage 2 (details in D’Eugenio et al., in prep.).

- We applied the `CUBE_BUILD` step to produce combined data cubes with a spaxel size of $0.1''$, using the exponential modified Shepard method (EMSM) weighting. This provides high signal-to-noise at the spaxel level yet slightly lower spatial resolution with respect to other weightings; the loss in resolution is compensated by the fact that these cubes are less affected by oscillations in the extracted spectra due to re-sampling effects, for example (see Law et al. 2023; Perna et al. 2023, and Appendix C).

We modified the `CUBE_BUILD` script to fix an error affecting the drizzle algorithm, as implemented in the pipeline version 1.8.5 which was not released at the time of data reduction¹. Finally, we also modified the `PHOTOM` script, applying the corrections implemented in the same unreleased pipeline version², which allows us to infer more reasonable flux densities (i.e. a factor ~ 100 smaller with respect to those obtained with standard pipeline 1.8.2). To test this calibration we also reduced the data using an external flux calibration (details in Perna et al. 2023), and obtained consistent results.

A complete description of the data reduction process and the tests we have performed to ensure its robustness can be found in Perna et al. (2023).

2.3. Data analysis

2.3.1. Quasar and host integrated line fitting

To obtain our integrated quasar spectrum, we integrated our data cube across an aperture of radii $0.35''$ for the wavelengths bluewards of the detector gap, and $0.45''$ redwards of the gap. These apertures were chosen by examining the PSF structure around $H\alpha$ and $H\beta$. These aperture radii contain the central peak of the PSF, but not the ring of reduced flux that occurs prior to the second radial PSF peak. This allowed us to maximise our signal to noise, while containing the majority of the quasar flux.

We compared the flux in this aperture to the total flux in the image (to radius $1.5''$) at the peak $H\alpha$ and $H\beta$ wavelengths, finding an average fraction for both quasars of 81.4% at $H\beta$, and 86.6% at $H\alpha$. We used these percentages as our flux correction, multiplying the integrated aperture flux bluewards of the detector gap by 1.228 and the integrated flux redwards of the detector gap by 1.155.

To fit our quasar spectra we used the Markov chain Monte Carlo (MCMC)-based technique of QUBESPEC³. Our quasar spectra contain $H\beta$ and $H\alpha$ emission from the BLR, which are blended with the narrow galaxy $H\beta$, $[\text{O III}] \lambda\lambda 4959, 5007$, and $H\alpha$ lines (galaxy narrow: ‘GN’), and also with broader lines

¹ `CUBE_BUILD` code changes in <https://github.com/spacetelescope/jwst/pull/7306>

² `PHOTOM` code changes in <https://github.com/spacetelescope/jwst/pull/7319>

³ <https://github.com/honzascholtz/Qubespec>

from the galaxy associated with a kinematically distinct component (e.g. an outflow; galaxy broad: ‘GB’). We note that we saw no evidence for any [N II] $\lambda\lambda 6548, 6583$ emission in our cubes, from either the quasar or the host galaxies and companions, and so we did not include an [N II] $\lambda\lambda 6548, 6583$ line in our fit. This likely indicates a low metallicity for our sources.

For the $H\alpha$ and $H\beta$ lines, we found that the BLR signal cannot be well fit with a single Gaussian. We instead fit the BLR $H\alpha$ and $H\beta$ lines with a broken power law,

$$f(x) = \begin{cases} (x/x_{\text{break}})^{-\alpha_1} & : x < x_{\text{break}} \\ (x/x_{\text{break}})^{-\alpha_2} & : x > x_{\text{break}} \end{cases} \quad (1)$$

that is convolved with a Gaussian with standard deviation σ (as in e.g. Nagao et al. 2006; Cresci et al. 2015). In our spectral fit we assumed that the galaxy lines were composed of a narrow component (GN), as well as a broad component (GB), which is typically blueshifted and therefore generates a wing in the total profile, which could be attributed to ionised gas outflows. For the two kinematic components, GN and GB, we fit each of the [O III] $\lambda\lambda 4959, 5007$ and $H\beta$ lines with a Gaussian with velocity offset and line widths equal in velocity space, as each of these lines likely arise from the same physical region with similar kinematics. We tied the amplitude of [O III] $\lambda 4959$ to be three times less than that of [O III] $\lambda 5007$, for both GN and GB components. The quasar continuum was modelled as a power law.

The $H\alpha$ line was fit separately after the [O III] $\lambda\lambda 4959, 5007$ – $H\beta$ complex. The GN $H\alpha$ component was constrained to have the same velocity as the [O III] $\lambda\lambda 4959, 5007$ lines. For the $H\alpha$ GN line width, the $H\alpha$ GB velocity offset and line width, and the $H\alpha$ BLR velocity and slopes α_1 and α_2 , the initial guess was the respective $H\beta$ fit property, with normally distributed priors surrounding that value. This is again because the lines likely arise from the same physical region with similar kinematics. We also chose an initial guess for the $H\alpha$ GN, GB, and BLR peak values to be 3.5 times that of the respective $H\beta$ values, with normally distributed priors around that value, which helps the fit to converge on a $H\alpha$ model that has realistic flux ratios relative to $H\beta$. Despite the $H\beta$ –[O III] $\lambda\lambda 4959, 5007$ and the $H\alpha$ complexes being fit independently, the agreement among the various kinematic properties was excellent, particularly for the host components (see Table 1). However, for VDES J0020–3653 we note that the $H\alpha$ BLR full width at half maximum (FWHM) is 3092^{+39}_{-1} km s^{−1}, which is significantly lower than the $H\beta$ FWHM of 4461^{+233}_{-182} km s^{−1}. This discrepancy may be due to the $H\alpha$ line being inaccurately measured as it lies close to the edge of the wavelength coverage of the detector; we are more confident in the $H\beta$ line measurement. There are also fit degeneracies which could be affecting this measurement.

We show the full integrated quasar spectrum for DELS J0411–0907 and VDES J0020–3653 in Fig. 1. In Fig. 2 we show the $H\beta$ and $H\alpha$ regions of these integrated spectra, alongside the best-fitting model. The velocity offset and FWHM for each of the model components are given in Table 1, and the resulting BLR line fluxes and luminosities are given in Table 2.

2.3.2. Continuum subtraction

To further analyse our quasar data cubes, we first subtracted the continuum emission from the spectra in each spaxel, by considering the flux in the continuum windows at rest frame 3790–3810 Å, 4210–4230 Å, 5080–5100 Å, 5600–5630 Å and 5970–6000 Å, following Kuraszekiewicz et al. (2002) and

Kovacevic et al. (2010); these windows are selected to be uncontaminated by emission lines and blended iron emission. We also added an additional continuum window at the red side of $H\alpha$ at the edge of the spectral range, at 5.260–5.266 μm in the observed frame, as well as a window near the blue edge of the spectral range, at 2.975–2.990 μm in the observed frame, to better constrain the continuum. We calculated the signal-to-noise ratio (S/N) at each wavelength in each spaxel, taking the noise to be the ‘ERR’ cube produced by the pipeline. For each spaxel in which the median S/N within these continuum windows is greater than 2, we interpolated between these continuum windows using SCIPY’s INTERP1D function using a spline interpolation of second order; this was found to be more robust than fitting a power law curve in each spaxel. In each of these spaxels the interpolation was subtracted from the spectra to create our continuum-subtracted cube. Figure 1 shows the original and continuum-subtracted spectrum of the brightest quasar spaxel.

We note that for VDES J0020–3653 there may be some broad $H\alpha$ flux in this reddest continuum window in the brightest quasar spaxels, as at this redshift the IFU spectral coverage does not extend to the pure continuum region redwards of $H\alpha$. However, we found that this window was necessary for finding a reasonable fit to the continuum around $H\alpha$. To reduce any potential effect of this on our results, we used the full, non-continuum subtracted cube in Sect. 2.3.1 when we fit our integrated quasar model to investigate the broad line properties. With our QubeSpec modelling we fit the emission lines as well as the continuum in the form of a power law. As the integrated quasar spectrum is well described by a power law, this approach does not require the continuum window strategy used here. In contrast, within individual spaxels the continuum is not well described by a power law due to the spatial variation of the PSF with wavelength, and so this continuum window approach is more reliable. For our spatially resolved analysis we are primarily interested in the narrow line emission, which is further from the edge of the detector, and so this should be less biased by this issue. However, we do caution that at this high redshift, the $H\alpha$ measurement of VDES J0020–3653 could be generally susceptible to edge effects from the detector and an imperfect continuum subtraction.

2.3.3. Quasar subtraction

In order to fully understand our quasar–host systems, we decomposed the observed emission into its various components. The aim is to subtract the bright unresolved flux from the quasar, revealing the extended narrow line emission from the host galaxy.

The full cube contains broad line emission from the quasar’s broad-line region (BLR) surrounding the black hole, for example from the $H\alpha$ and $H\beta$ lines. The BLR is spatially unresolved at these redshifts, and thus this broad line emission is spread spatially according to the PSF of the instrument. In our BLR Quasar Subtraction method (see below), we subtract this BLR component from the cube. The remaining flux in the cube is narrow line emission, for example from [O III] $\lambda\lambda 4959, 5007$ as well as the $H\alpha$ and $H\beta$ lines which also have a strong broad component. This narrow emission is emitted both by the quasar’s narrow line region (NLR), photoionised by the AGN and shocks, as well as gas throughout the extended host galaxy (and any companion galaxies) which is photoionised by star formation. While the NLR can be spatially extended, significant NLR emission is produced by the spatially unresolved central region surrounding the AGN, and so this component will clearly trace out the PSF

Table 1. Measured line velocity offsets and velocity dispersions (relative to the quoted redshift) from the integrated quasar spectra.

	GN ([O III], H β)	GB ([O III], H β)	BLR, H β	GN, H α	GB, H α	BLR, H α
DELS J0411–0907						
V_r (km s $^{-1}$)	0 [$z = 6.818$]	-404 ± 24	317^{+69}_{-64}	0	-398 ± 5	338 ± 7
FWHM (km s $^{-1}$)	685 ± 32	1784 ± 39	3404^{+55}_{-155}	700 ± 10	1780 ± 6	2794^{+1}_{-39}
VDES J0020–3653						
V_r (km s $^{-1}$)	0 [$z = 6.855$]	-530 ± 42	181^{+65}_{-73}	0	-492 ± 5	159 ± 8
FWHM (km s $^{-1}$)	541^{+110}_{-84}	2439 ± 73	4461^{+233}_{-182}	646 ± 9	2429 ± 5	3092^{+39}_{-1}

Notes. The FWHM have been corrected for instrumental broadening ($\text{FWHM}_{\text{inst,H}\beta} = 115 \text{ km s}^{-1}$, $\text{FWHM}_{\text{inst,H}\alpha} = 85 \text{ km s}^{-1}$, Jakobsen et al. 2022).

shape. To understand the true spatial extent and kinematics of the extended narrow line emission, and not be biased by the bright unresolved NLR emission, we subtract this narrow unresolved flux from our cube. This is our Narrow & Broad (N&B) Quasar Subtraction, as detailed below.

To separate the host and quasar emission, we used the code QDeblend3D (Husemann et al. 2013, 2014), which uses the relative strength of quasar broad lines in each spaxel to map out the spatial PSF. This strategy allows us to use the specific quasar observation to create an accurate PSF model, instead of relying on an external observation of a known point source (i.e. star) or a theoretical PSF model. The spatial PSF varies with the precise position of the source on the detectors, the general position on the sky, and time, so matching the PSF of our specific observations with a PSF observation or model is less precise than the broad line model we can create here. This methodology has successfully been used for IFU observations of lower-redshift quasar host galaxies (e.g. Husemann et al. 2013, 2014; Vayner et al. 2016; Kakkad et al. 2020).

As the NIRSpec PSF varies with wavelength, we opted to perform the quasar subtraction at two different wavelength regimes. For the spectra bluewards of the detector gap, we used the H β line for the subtraction, and for the spectra redwards of the detector gap we used the H α line for subtraction. This allows for the best subtraction for the wavelength region around each of these two lines.

Step 1, Spatial PSF model. We determined the spatial PSF shape by measuring the relative flux of the quasar BLR at each spatial location. The BLR is spatially unresolved and thus this emission will trace the PSF shape of the instrument. To measure this relative flux we used the continuum-subtracted cube. For H α , we took the mean of the flux between rest-frame 6500–6523 Å and 6592–6615 Å, either side of the peak of H α . These broad spectral windows are free from any narrow lines, which would bias the measurement; they are marked in Fig. 3, which shows an example of this quasar subtraction process. For H β , the equivalent was performed for emission between rest frame 4800–4830 Å and 4880–4910 Å. Once this broad line flux was measured in each spatial pixel, it was normalised to that of the central brightest quasar spaxel, giving a 2D fractional map of the relative flux of the spatially unresolved BLR, that is, the 2D PSF.

To identify spaxels with significant quasar flux from the PSF model, we calculated the S/N in each individual wavelength channel across the selected broad spectral window for each spaxel, using the ‘ERR’ extension as the noise. For our final PSF shape, we selected spaxels in which at least three consecutive wavelength channels had $S/N > 10$, and then expanded this region spatially by selecting any adjacent spaxels with $S/N > 2$ over two consecutive wavelength channels, following

the FIND_SIGNAL_IN_CUBE algorithm of Sun (2020; see also Sun et al. 2018). To reduce the effect of any artefacts and companion galaxies on the measured PSF shape, we cut the PSF at 10σ , where $\sigma = \text{FWHM}/(2\sqrt{2\log 2})$ and the FWHM is the diffraction limit of the telescope at the observed wavelength of H β and H α , 0.146'' and 0.201'' respectively. This ensures we are only performing the quasar subtraction in regions that have a broad line signal, while ensuring we extract as much of the quasar as possible. The resulting masked PSF shapes are shown in Fig. A.1, for both the H α and H β subtractions for both quasars. Measuring the FWHM of the resulting H β PSFs gives 0.18'' for VDES J0020–3653 and 0.16'' for DELS J0411–0907, and 0.23'' for H α for both VDES J0020–3653 and DELS J0411–0907, consistent with expectations for the PSF size.

Step 2, Quasar spectral model. To perform the quasar subtraction we required a 3D quasar model cube to subtract from the initial quasar and host cube. To create a 3D cube for the quasar emission, alongside the PSF shape (spatial x, y dimensions) we also needed a model for the quasar spectrum (spectral λ dimension), for which we considered two approaches. The first approach was to use the observed spectrum of the brightest spaxel, the centre of the quasar emission, under the assumption that the host line emission is negligible. We refer to this as the ‘N&B Quasar Subtraction’, as this quasar cube includes both the narrow (N) and broad (B) components of the central spectrum, and so both components are subtracted. Our second approach was to use a model of the BLR component of the quasar spectrum. We took this model from our fit to the integrated quasar spectrum (the red curve in Fig. 2, with values quoted in Table 1). This quasar model only includes the BLR component of the fit, and so we refer to this as the ‘BLR Quasar Subtraction’ as only the BLR emission is subtracted from the initial cube. Our process for integrating and fitting the quasar spectrum is described in detail in Sect. 2.3.1.

In our quasar subtraction, the spatial variation of the quasar’s BLR flux was used to determine the PSF shape. However, the N&B subtraction subtracts both the broad and narrow emission that were present in the central quasar spaxel. These emission lines are emitted from the central, unresolved NLR, which is spread according to the PSF shape. This N&B subtraction results in a clear view of the narrow line flux in the underlying, spatially extended host galaxy, without contamination from the bright lines from the central NLR region that have been smeared by the PSF shape. This is ideal for measurements of the spatial distribution and kinematics of emission line regions, as well as measurements of the SFRs which would otherwise be significantly biased by the large amount of AGN-photoionised flux in the centre. However, this method uses the spectrum from

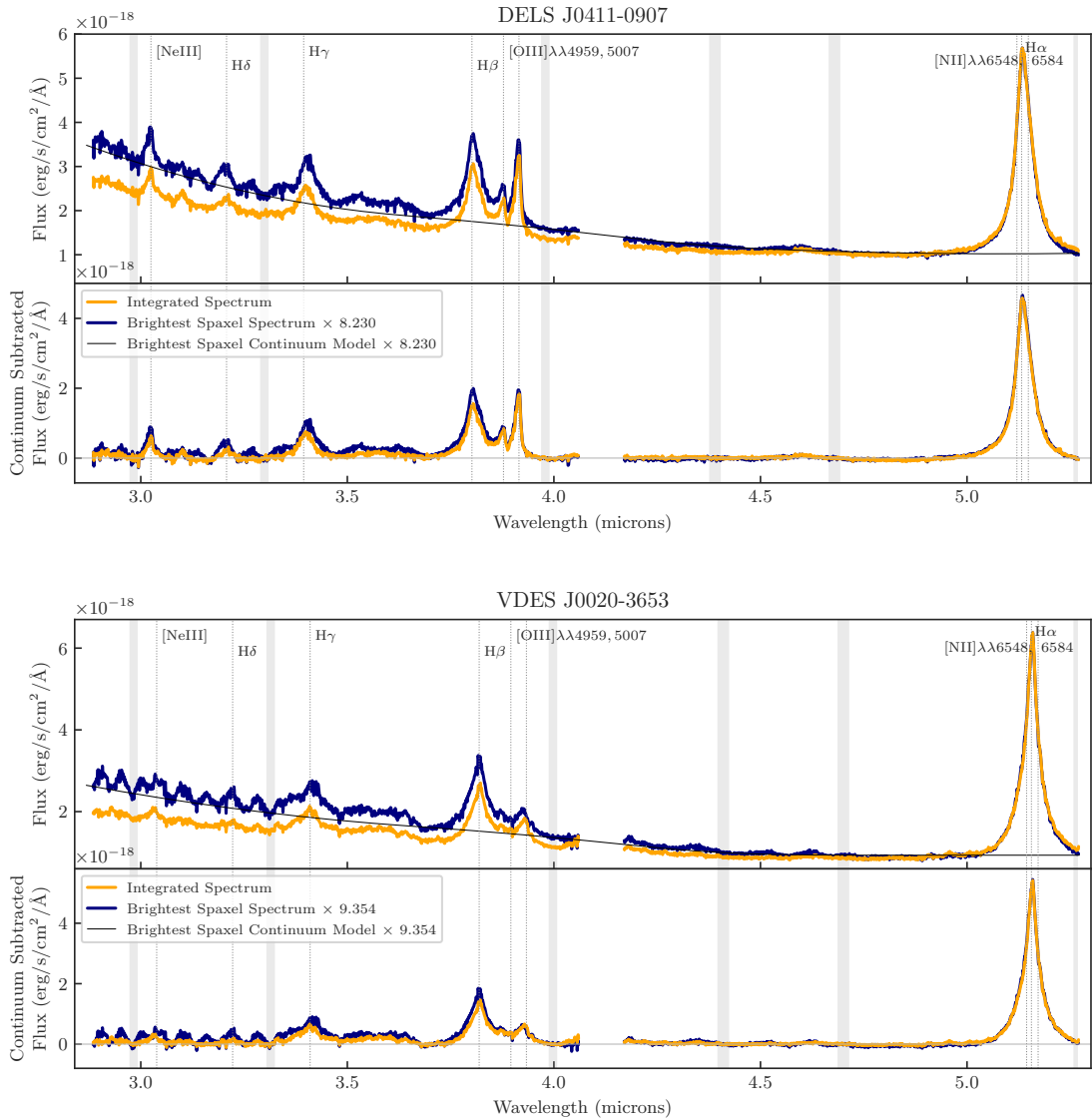
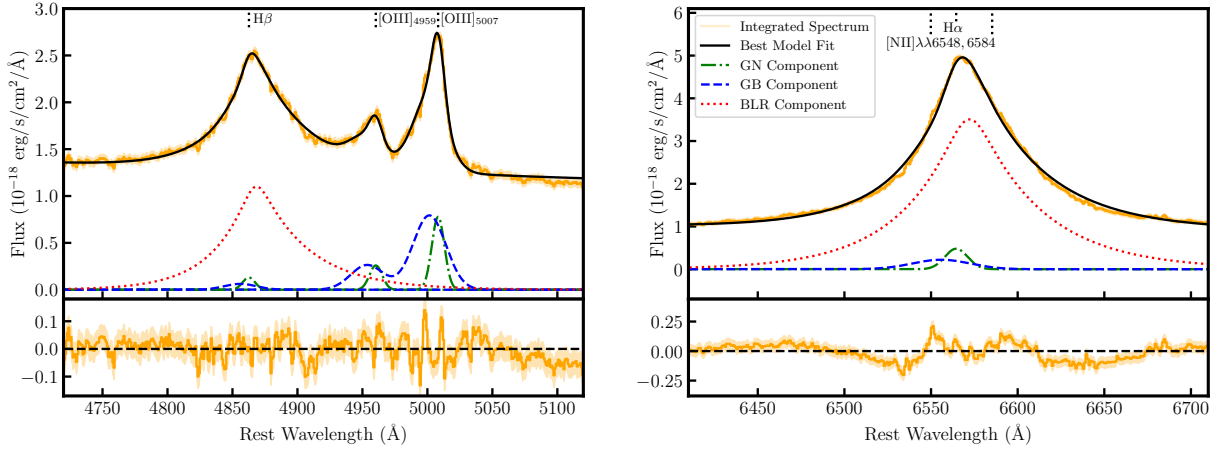


Fig. 1. Quasar spectrum for DELS J0411–0907 (top) and VDES J0020–3653 (bottom), showing the spectrum from the brightest spaxel (navy), alongside the integrated spectrum (orange). The integrated spectrum was integrated over a radius of $0.35''$ for the wavelengths bluewards of the detector gap, and $0.45''$ redwards of the gap, corresponding to the apertures selected for our quasar fitting (Sect. 2.3.1). Our flux corrections of 81.4% and 86.6% have been applied to the integrated spectrum. The spectrum of the brightest spaxel is increased by a constant scaling factor, 8.230 for DELS J0411–0907 and 9.354 for VDES J0020–3653, such that the peak of $H\alpha$ is equal for both spectra in the plots. The lower panel in each shows the spectra after continuum subtraction. For the brightest spaxel spectrum, the continuum model subtracted from the spectrum is shown in black in the top panel. For the continuum-subtracted integrated spectrum in the lower panel, the integration was performed on the continuum-subtracted cube (i.e. the continuum subtraction was first performed on each of the spaxels individually). The dotted grey vertical lines depict lines of interest at the redshift of the quasar ($z = 6.854$ for VDES J0020–3653 and $z = 6.818$ for DELS J0411–0907), and the grey regions show the continuum windows. The detector gap from 4.06 to $4.17 \mu\text{m}$ has been masked. We note that some minor oscillations are present in the single spaxel spectrum (navy), which can be particularly noticed below $3.3 \mu\text{m}$ in the single spaxel spectrum. These are caused by spatial undersampling of the PSF, which is a known issue when considering spectra in individual NIRSpect IFU spaxels; we describe this in detail in Perna et al. (2023). When measuring the quasar properties in Sect. 3.1, we used the integrated spectrum (orange), thus removing these single pixel effects. For the quasar subtraction, we found the best performance using the single spaxel spectrum (navy), however these oscillations do not significantly affect our results which directly focus on the regions around $H\alpha$ and $H\beta$.

the individual brightest quasar spaxel, and so can be subject to observational artefacts that would be removed when integrating over a larger region, for example oscillations in the spectra (see Perna et al. 2023). We chose to use the individual spaxel spectrum and not an integrated spectrum for the model as we found that this resulted in the best quasar subtraction. This model also assumes that the host contribution to the line flux in this central spaxel is negligible, while there may be some small contribution at the position of the optical lines analysed in this work.

In contrast, the BLR quasar subtraction method allows us to view the complete narrow line emission maps, including the contribution of the central unresolved NLR. Our BLR subtraction technique subtracts only the BLR quasar flux, with all of the narrow flux from the central core remaining. Much of this remaining narrow line flux is spread according to the PSF shape, which significantly contaminates any spatial analysis of the extended host region. This approach is also model dependent, varying based on the BLR model fit to the integrated quasar

DELS J0411–0907



VDES J0020–3653

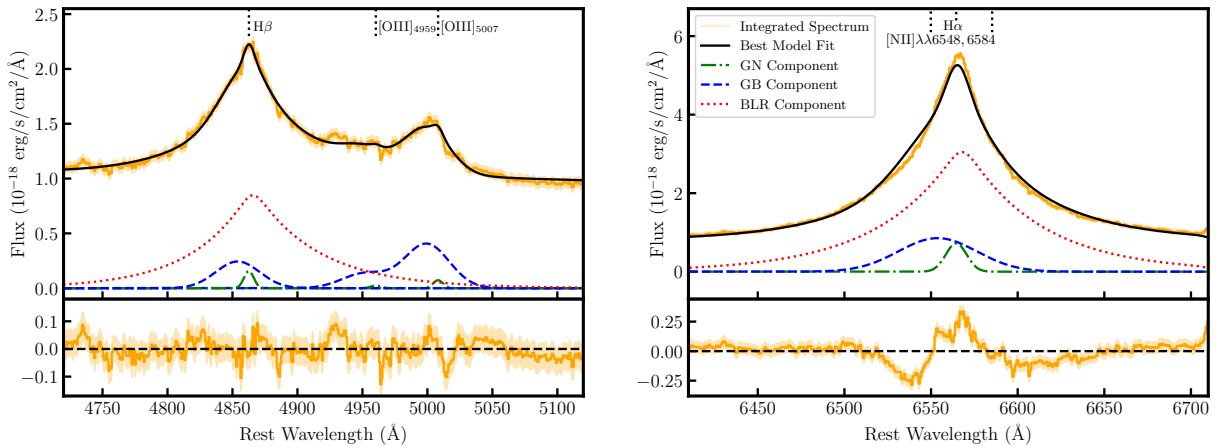


Fig. 2. Integrated quasar spectra for DELS J0411–0907 (top) and VDES J0020–3653 (bottom) (orange curve), showing the regions around $H\beta$ (left) and $H\alpha$ (right). The integrated spectrum was integrated over a radius of $0.35''$ for the wavelengths bluewards of the detector gap, and $0.45''$ redwards of the gap, corresponding to the apertures selected for our quasar fitting (Sect. 2.3.1). No flux correction has been applied. The best model fit (black) is shown alongside the narrow GN line components (green dot-dashed), the broader GB components (blue dashed lines), and the broken power law component for the BLR (red dotted lines). The lower panels show the residual of the model fit.

spectrum. With their various advantages and disadvantages, we used both approaches throughout this work.

Step 3, Subtracting the 3D PSF model. For each of these choices for the model quasar spectrum, we scaled the quasar spectrum by the 2D PSF to create a 3D quasar cube. We then subtracted this quasar cube from the original cube, revealing our estimate of the host galaxy’s 3D spectrum. We visually inspected the quasar model fit and residual for a range of spaxels to confirm our subtraction is robust; an example for one spaxel is shown in Fig. 3.

2.3.4. Host line maps

To estimate the noise for our host galaxy maps, we considered that the quasar subtraction introduces additional noise to the resulting host cube that should be accounted for. Following a Monte Carlo process, we generated 200 different realisations of the continuum-subtracted cube with normally distributed noise, where σ was

taken from the ‘ERR’ extension from the original cube. We then performed the $H\alpha$ and $H\beta$ quasar subtraction on each of these 200 cube realisations. To create our modified noise cube, we calculated the standard deviation of these 200 realisations of the quasar subtracted cube at each wavelength in each spaxel.

For the $H\beta$ –[O III] $\lambda\lambda 4959, 5007$ line complex the values in these noise maps are up to 34% higher than the original noise maps in the central spatial regions of the quasar for the N&B quasar subtraction, and 4% higher for the BLR subtraction. For the $H\alpha$ line, the values in the noise map are up to 47% higher than the original noise map for the N&B quasar subtraction, and 10% higher for the BLR subtraction. The N&B subtraction introduces more noise than the BLR subtraction, as the N&B quasar model spectrum contains noise while the BLR quasar spectrum is a smooth model and the model uncertainties are not considered in this calculation. The quasar subtraction adds additional uncertainty, particularly where more quasar flux has to be subtracted.

Table 2. Fluxes and luminosities measured for the 5100 Å continuum, H α and H β BLR lines, alongside the derived black hole masses and Eddington ratios using these properties.

	DELS J0411–0907	VDES J0020–3653
$F_{5100}(10^{-18} \text{ erg s}^{-1} \text{ cm}^{-2} \text{ \AA}^{-1})$	1.40 ± 0.02	1.18 ± 0.01
$F_{H\alpha}(10^{-16} \text{ erg s}^{-1} \text{ cm}^{-2})$	$26.4^{+0.2}_{-0.3}$	$25.9^{+0.2}_{-0.2}$
$F_{H\beta}(10^{-16} \text{ erg s}^{-1} \text{ cm}^{-2})$	8.0 ± 0.3	$8.3^{+0.5}_{-0.4}$
$\lambda L_{5100}(10^{46} \text{ erg s}^{-1})$	3.2 ± 0.2	2.7 ± 0.2
$L_{H\alpha}(10^{44} \text{ erg s}^{-1})$	$14.9^{+0.1}_{-0.2}$	14.8 ± 0.1
$L_{H\beta}(10^{44} \text{ erg s}^{-1})$	4.5 ± 0.2	4.7 ± 0.3
$M_{\text{BH,H}\beta,5100}(10^9 M_{\odot})$ (G)	$2.0^{+3.4}_{-1.3}$	$3.1^{+5.3}_{-2.0}$
$M_{\text{BH,H}\beta,5100}(10^9 M_{\odot})$ (V)	$1.7^{+2.8}_{-1.1}$	$2.7^{+4.5}_{-1.7}$
$M_{\text{BH,H}\beta}(10^9 M_{\odot})$ (G)	$1.3^{+2.1}_{-0.8}$	$2.3^{+3.9}_{-1.5}$
$M_{\text{BH,H}\beta}(10^9 M_{\odot})$ (V)	$2.5^{+4.3}_{-1.6}$	$4.5^{+7.7}_{-2.9}$
$M_{\text{BH,H}\alpha}(10^9 M_{\odot})$	$0.9^{+1.6}_{-0.6}$	$1.1^{+1.9}_{-0.7}$
$L_{\text{Bol}}/L_{\text{Edd,H}\beta,5100}$ (G)	$0.7^{+0.4}_{-0.3}$	$0.3^{+0.2}_{-0.1}$
$L_{\text{Bol}}/L_{\text{Edd,H}\beta,5100}$ (V)	$0.9^{+0.5}_{-0.4}$	0.4 ± 0.2
$L_{\text{Bol}}/L_{\text{Edd,H}\beta}$ (G)	$1.2^{+0.7}_{-0.5}$	$0.5^{+0.3}_{-0.2}$
$L_{\text{Bol}}/L_{\text{Edd,H}\beta}$ (V)	$0.6^{+0.3}_{-0.2}$	0.2 ± 0.1
$L_{\text{Bol}}/L_{\text{Edd,H}\alpha}$	$1.6^{+1.0}_{-0.7}$	$0.9^{+0.6}_{-0.4}$

Notes. The errors for the black hole masses and Eddington ratios include the fit uncertainties as well as the 0.43 dex uncertainty due to the intrinsic scatter in the scaling relations. We note that all flux uncertainties are measurement uncertainties and do not include any intrinsic uncertainty in the flux level from the data calibration. The two sets of $M_{\text{BH,H}\beta,5100}$ and $M_{\text{BH,H}\beta}$ and corresponding Eddington ratios refer to the calculations using Eqs. (3) and (4) for the Greene & Ho (2005) and Vestergaard & Peterson (2006) coefficients; these are marked with a ‘G’ and ‘V’ respectively.

To create maps of the H α , H β , and [O III] $\lambda\lambda 4959, 5007$ emission of the host galaxy, we fit the spectrum in each spaxel as a series of Gaussians, using ASTROPY’s Levenberg–Marquardt algorithm. We assumed that the narrower galaxy lines are composed of a narrow component (GN) as well as a broader wing (GB; see Sect. 2.3.1). For the GN and GB components, we fit each of the four lines as a Gaussian with mean velocity and line widths equal in velocity space. We tied the amplitude of [O III] $\lambda 4959$ to be three times less than that of [O III] $\lambda 5007$, for both the GN and GB components. These theoretical flux ratio constraints provide a good fit for the host galaxy [O III] $\lambda\lambda 4959, 5007$ lines for both the N&B and BLR quasar subtraction, which gives further confidence in our subtraction techniques. As noted above, we saw no evidence for any [N II] $\lambda\lambda 6548, 6583$ emission in our cubes, and did not include those lines in our fit.

When the spectrum can be well fit with two Gaussians, the Gaussian with the smallest velocity dispersion σ was assigned as the GN component, while the largest was assigned to the GB component. When only one Gaussian was preferred, if it had $\sigma \leq 33 \text{ \AA}$, or approximately 600 km s^{-1} , it was assigned as a GN component, otherwise as a GB component.

To determine the flux of each of the GN and GB line components we integrated the individual Gaussian model. The S/N was calculated by integrating the noise cube, calculated from the quasar subtraction algorithm, across the same spectral region. Using these noise maps we searched for spaxels with $S/N > 5$, and then expanded this region spatially by selecting any adjacent

spaxels with $S/N > 1.5$, following the FIND_SIGNAL_IN_CUBE algorithm of Sun (2020). In the maps we only display spaxels meeting this criterion. The resulting maps are shown in Figs. 4 and 6 for the N&B subtraction for DELS J0411–0907 and VDES J0020–3653 respectively, with the BLR subtraction maps for both quasars shown in Fig. B.1 to show the differences between the two subtraction methods.

To create velocity maps, we calculated the median velocity v_{50} , a non-parametric measure for the line centre. For the velocity dispersion maps, we calculated w_{80} , the width containing 80% of the line flux. This is a non-parametric measure, which is approximately equal to the FWHM for a Gaussian line ($w_{80} = 1.088 \text{ FWHM}$; see e.g. Zakamska & Greene 2014). The velocity dispersion maps are derived after removing the instrumental width in quadrature at each spaxel, where for NIRSpect in the G395H/F290LP configuration, $\text{FWHM}_{\text{inst,H}\beta} \approx 115 \text{ km s}^{-1}$, and $\text{FWHM}_{\text{inst,H}\alpha} \approx 85 \text{ km s}^{-1}$ for the redshift of these quasars (Jakobsen et al. 2022). These velocity and velocity dispersion maps are also shown in Figs. 4 and 6 for the N&B subtraction, with the BLR subtraction maps also presented in Fig. B.1.

3. Results

3.1. Black hole properties

3.1.1. Redshift

We show the integrated quasar spectrum for DELS J0411–0907 and VDES J0020–3653 in Fig. 2, with the parameters from our spectral fit given in Table 1.

We derived the quasar redshift based on the galaxy narrow (GN) [O III] $\lambda 5007$ emission. For DELS J0411–0907, we found a redshift of $z = 6.818 \pm 0.001$. This is broadly in agreement with the Lyman- α redshift of DELS J0411–0907, $z_{\text{Ly}\alpha} = 6.81 \pm 0.03$ (Pons et al. 2019; Wang et al. 2019), and the Mg II redshift, $z_{\text{Mg II}} = 6.824$ (Pons et al. 2019).

For VDES J0020–3653, the quasar redshift based on the narrow (GN) [O III] $\lambda 5007$ emission is $z = 6.855 \pm 0.002$. In comparison, the Lyman- α redshift of VDES J0020–3653 is $z_{\text{Ly}\alpha} = 6.86 \pm 0.01$ and the Mg II redshift is $z_{\text{Mg II}} = 6.834 \pm 0.0004$ (Reed et al. 2019). For VDES J0020–3653, there is a significant blueshift of Mg II compared to the [O III] $\lambda 5007$ and Lyman- α lines.

3.1.2. Black hole masses

Black hole masses can be estimated using the virial relation:

$$M_{\text{BH}} = \frac{fR\Delta V^2}{G} \quad (2)$$

where R is the size of the BLR, ΔV is the width of the emission line, G is the gravitational constant and f is a scale factor. To robustly determine the BLR size R , reverberation mapping studies measure the time delay τ of variability in the emission line to the continuum region, with $R = c\tau$, where c is the speed of light. Empirical correlations have been found between τ and the continuum luminosity of the quasar (e.g. Kaspi et al. 2000), with $R \propto L^\gamma$, allowing the black hole mass to be estimated from single-epoch measurements.

For this work we used the empirically derived relation:

$$M_{\text{BH,H}\beta,5100\text{\AA}} = a \left(\frac{\lambda L_{5100\text{\AA}}}{10^{44} \text{ erg s}^{-1}} \right)^b \left(\frac{\text{FWHM}_{\text{H}\beta}}{10^3 \text{ km s}^{-1}} \right)^2 M_{\odot}, \quad (3)$$

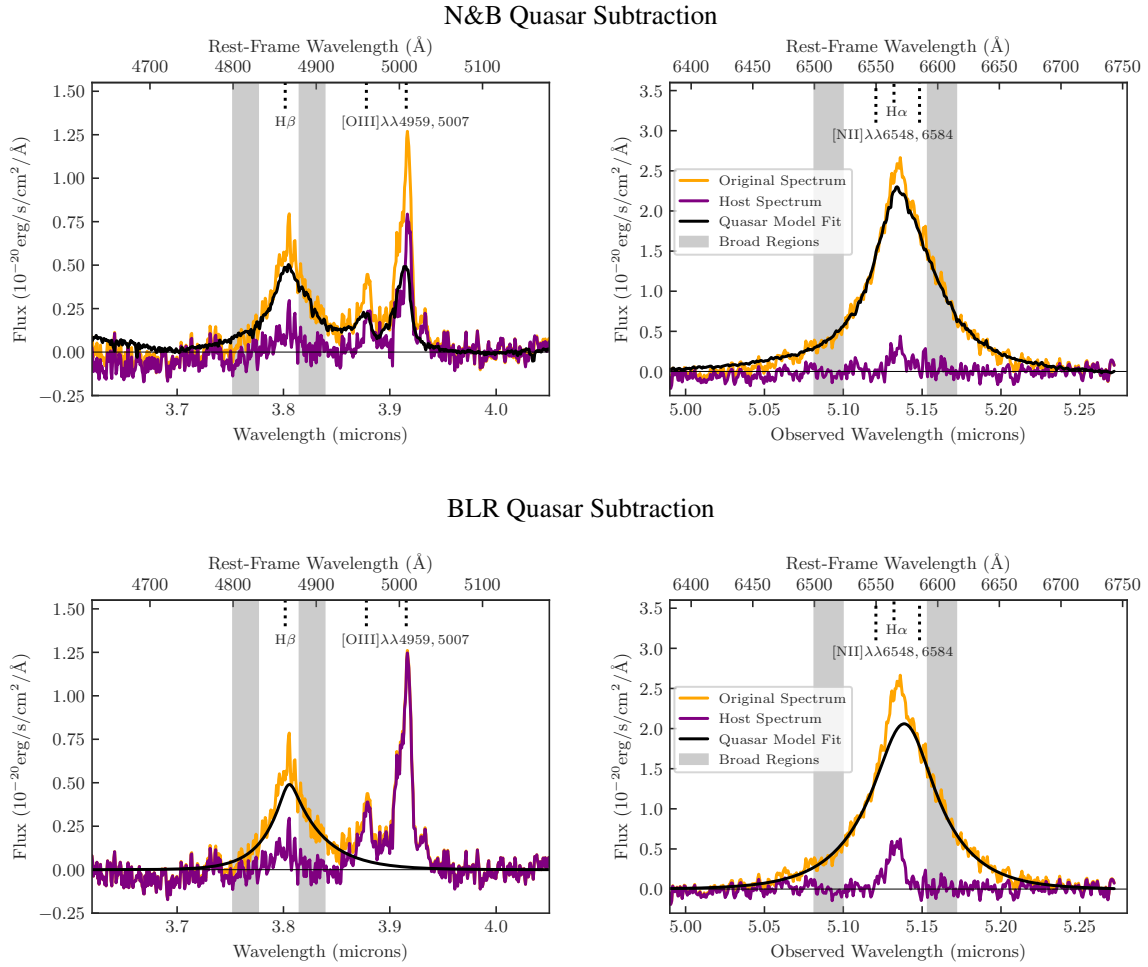


Fig. 3. Visualisation of the quasar subtraction using the broad $H\beta$ (left) and $H\alpha$ (right) lines from DELS J0411–0907. This shows the spectrum in spaxel (23, 24), with the quasar peak located at spaxel (26, 24), in image coordinates. The orange spectrum is the original continuum-subtracted spectrum in the spaxel, containing line flux from both the quasar and host galaxy. The black line is the quasar model spectrum. The top panels show the choice that the quasar model spectrum is that of the central brightest quasar spaxel, which contains both narrow and broad emission – the N&B subtraction. The bottom panel shows the choice that the quasar model spectrum is from our best-fit model to the quasar spectrum (Fig. 2) – the BLR subtraction. Using the broad spectral windows marked in grey, the quasar model (black) was scaled to fit the combined spectrum (orange). The purple spectrum shows the residual to that fit, which is the host spectrum.

where [Greene & Ho \(2005\)](#) calibrate the constants a and b to be $a = (4.4 \pm 0.2) \times 10^6$, $b = 0.64 \pm 0.02$, while alternatively [Vestergaard & Peterson \(2006\)](#) derived $a = (8.1 \pm 0.4) \times 10^6$, $b = 0.50 \pm 0.06$. For the quasars under study we measured the continuum-luminosity at rest-frame 5100 \AA , $L_{5100 \text{ \AA}}$, from our integrated quasar spectrum, taking the mean value between $5090\text{--}5110 \text{ \AA}$ to account for noise variations, and using the best-fit redshift of the quasar $[\text{O III}] \lambda\lambda 4959, 5007$ emission (Sect. 3.1.1). Using this and our $H\beta$ broad line FWHM, we calculated the black hole masses using Eq. (3) for both the [Greene & Ho \(2005\)](#) and [Vestergaard & Peterson \(2006\)](#) correlations, which we present in Table 2.

However, the continuum luminosity can be difficult to measure due to contamination by Fe II lines and, for lower luminosity quasars, the host galaxy itself. To circumvent this, [Greene & Ho \(2005\)](#) and [Vestergaard & Peterson \(2006\)](#) derived empirical relations for estimating the black hole mass based solely on the $H\beta$ emission lines:

$$M_{\text{BH},H\beta} = a \left(\frac{L_{H\beta}}{10^{42} \text{ erg s}^{-1}} \right)^b \left(\frac{\text{FWHM}_{H\beta}}{10^3 \text{ km s}^{-1}} \right)^2 M_{\odot} \quad (4)$$

where [Greene & Ho \(2005\)](#) estimate $a = (3.6 \pm 0.2) \times 10^6$, $b = 0.56 \pm 0.02$, while [Vestergaard & Peterson \(2006\)](#) derived $a = (4.7 \pm 0.3) \times 10^6$, $b = 0.63 \pm 0.06$. [Greene & Ho \(2005\)](#) also derived a correlation based on the $H\alpha$ broad line:

$$M_{\text{BH},H\alpha} = (2.0^{+0.4}_{-0.3}) \times 10^6 \times \left(\frac{L_{H\alpha}}{10^{42} \text{ erg s}^{-1}} \right)^{0.55 \pm 0.02} \left(\frac{\text{FWHM}_{H\alpha}}{10^3 \text{ km s}^{-1}} \right)^{2.06 \pm 0.06} M_{\odot}. \quad (5)$$

Using our measured $H\beta$ and $H\alpha$ broad line properties, we calculated the black hole masses using Eqs. (4) and (5) for both the [Greene & Ho \(2005\)](#) and [Vestergaard & Peterson \(2006\)](#) correlations. These are also listed in Table 2.

As these empirical black hole mass relations have large scatter, we took the error in these relations to be 0.43 dex, the quoted scatter from [Vestergaard & Peterson \(2006\)](#), and added this in quadrature with our measurement uncertainty from the MCMC fit.

DELS J0411–0907. For DELS J0411–0907, we found that the various scaling relations (Eqs. (3)–(5)) give a black hole

mass between 0.9 and $2.5 \times 10^9 M_\odot$ (Table 2). These measures are all consistent within the uncertainties. We note that while the $H\beta-L_{5100\text{\AA}}$ black hole mass estimated by the [Greene & Ho \(2005\)](#) and [Vestergaard & Peterson \(2006\)](#) relations are similar, at 2.0 and $1.7 \times 10^9 M_\odot$ respectively, the pure $H\beta$ black hole mass estimates are quite different between the two versions of the relation. The [Greene & Ho \(2005\)](#) $H\beta$ relation gives a low black hole mass of $1.3 \times 10^9 M_\odot$, while the [Vestergaard & Peterson \(2006\)](#) relation gives $2.5 \times 10^9 M_\odot$, twice as large. This variation between the two scaling relations could be due to the brightness of this quasar, which is brighter than the quasars considered in those studies. We also note that the [Greene & Ho \(2005\)](#) $H\alpha$ black hole mass for DELS J0411–0907 is $0.9 \times 10^9 M_\odot$, the lowest of these estimates, yet this is consistent with the other estimates within the uncertainties. As the pure $H\beta$ and $H\alpha$ relations involve a further calibration from $L_{5100\text{\AA}}$ to $L_{H\alpha/H\beta}$, we opted to take the average of the two $M_{\text{BH},H\beta,5100\text{\AA}}$ measurements as our best black hole mass estimate: $(1.85^{+2}_{-0.8}) \times 10^9 M_\odot$. We reiterate that all of these black hole mass estimates are consistent with each other within the uncertainties.

In comparison, from the FWHM of the Mg II line and the rest-frame 3000\AA luminosity measured from Magellan FIRE spectra ([Pons et al. 2019](#)), the DELS J0411–0907 black hole mass derived using the [Vestergaard & Osmer \(2009\)](#) relation is $M_{\text{BH},\text{Mg II}} = (0.61 \pm 0.05) \times 10^9 M_\odot$. This is much lower than our measurements. This quoted error considers only measurement uncertainties, and does not include the additional ~ 0.55 dex uncertainty from the scatter in the scaling relation ([Vestergaard & Osmer 2009](#)), which would be $M_{\text{BH},\text{Mg II}} = (0.6^{+1.6}_{-0.4}) \times 10^9 M_\odot$. Alternatively, applying the [Shen et al. \(2011\)](#) relation to the same Mg II line FWHM and rest-frame 3000\AA luminosity from [Pons et al. \(2019\)](#), following [Farina et al. \(2022\)](#), we derived $M_{\text{BH},\text{Mg II}} = 0.95 \times 10^9 M_\odot$ for DELS J0411–0907. The Mg II line of this quasar was also observed with Keck NIRES, from which the black hole mass was estimated as $M_{\text{BH},\text{Mg II}} = (0.95 \pm 0.09) \times 10^9 M_\odot$ using the [Vestergaard & Osmer \(2009\)](#) relation ([Yang et al. 2021](#)), with an additional ~ 0.55 dex uncertainty from the scatter in the scaling relation— $M_{\text{BH},\text{Mg II}} = (1.0^{+2.4}_{-0.7}) \times 10^9 M_\odot$. While these Mg II black hole masses are all lower than our best estimates, when including the large uncertainty from the scatter in the scaling relations, all of the measurements are consistent.

In summary, the best estimate for the black hole mass of DELS J0411–0907 from NIRSspec IFU, $M_{\text{BH}} = (1.85^{+2}_{-0.8}) \times 10^9 M_\odot$, is larger than the existing measurements from Mg II, $M_{\text{BH},\text{Mg II}} = 0.6\text{--}1 \times 10^9 M_\odot$. Our measurements used the $H\beta$ – 5100\AA black hole mass relation with scatter of ~ 0.43 dex, compared with the larger ~ 0.55 dex scatter in the Mg II relation, highlighting the benefit of using these Balmer lines as black hole mass estimators.

VDES J0020–3653. For VDES J0020–3653, we found that the various scaling relations give a wide range of black hole mass estimates, between 1.1 and $4.5 \times 10^9 M_\odot$. These estimates are all consistent within the uncertainties. We note that the lowest measurement is the $H\alpha$ mass measurement of $1.1 \times 10^9 M_\odot$. For VDES J0020–3653, the $H\alpha$ line falls at the edge of the wavelength coverage of the detector, which could cause issues with this measurement. Thus the $H\beta$ measurements of $2.3\text{--}4.5 \times 10^9 M_\odot$ are likely more reliable, although all measurements are consistent. As the pure $H\beta$ and $H\alpha$ relations involve a further calibration from $L_{5100\text{\AA}}$ to $L_{H\alpha/H\beta}$, we opted to take the average of

the two $M_{\text{BH},H\beta,5100\text{\AA}}$ measurements as our best black hole mass estimate: $(2.9^{+3.5}_{-1.3}) \times 10^9 M_\odot$. We note again that the [Greene & Ho \(2005\)](#) and [Vestergaard & Peterson \(2006\)](#) black hole masses are quite different, with the [Greene & Ho \(2005\)](#) estimate larger for the $H\beta$ – $L_{5100\text{\AA}}$ relation, while the [Vestergaard & Peterson \(2006\)](#) mass is twice as large for the pure $H\beta$ relation. This variation could again be due to the brightness of this quasar, which is brighter than the quasars considered in those studies. We reiterate that all of these black hole mass estimates are consistent within the uncertainties.

In comparison, [Reed et al. \(2019\)](#) measured a black hole mass from the Mg II line and the rest-frame 3000\AA luminosity of $M_{\text{BH},\text{Mg II}} = (1.67 \pm 0.32) \times 10^9 M_\odot$, using the [Vestergaard & Osmer \(2009\)](#) relation. Accounting for the additional ~ 0.55 dex scatter in the Mg II black hole mass relation, this is $M_{\text{BH},\text{Mg II}} = (1.7^{4.3}_{-1.2}) \times 10^9 M_\odot$. Applying the [Shen et al. \(2011\)](#) relation to the same Mg II line FWHM and rest-frame 3000\AA luminosity from [Reed et al. \(2019\)](#), [Farina et al. \(2022\)](#) derived a larger $M_{\text{BH},\text{Mg II}} = 2.51 \times 10^9 M_\odot$. These estimates are in agreement with our estimated black hole mass of $(2.9^{+3.5}_{-1.3}) \times 10^9 M_\odot$.

For our two quasars, we found that VDES J0020–3653 has a $H\beta$ – $L_{5100\text{\AA}}$ black hole mass that is consistent with the existing Mg II black hole mass estimates, while the $H\beta$ – $L_{5100\text{\AA}}$ black hole mass for DELS J0411–0907 is larger than the Mg II estimates, albeit consistent within the large uncertainties. [Shen et al. \(2008\)](#) found that for ~ 8000 low- z SDSS quasars, $\log(M_{\text{BH},H\alpha}/M_{\text{BH},\text{Mg II}})$ follows a Gaussian distribution with mean of 0.034 and dispersion of 0.22 dex, generally indicating a good agreement yet with some quasars found to have significantly different values of $\log(M_{\text{BH},H\alpha}/M_{\text{BH},\text{Mg II}})$ up to ± 1.5 . While high- z quasars may follow a different distribution, our quasars are consistent with this [Shen et al. \(2008\)](#) scenario where Mg II and $H\beta$ mass estimates can be consistent, although for some quasars these estimates can vary significantly. This highlights the need for obtaining $H\beta$ and $H\alpha$ masses of a larger sample of high- z quasars with JWST, to more accurately measure black hole mass in the early Universe (see also [Yang et al. 2023a](#)).

3.1.3. Eddington ratios

We now consider the Eddington Ratio $\lambda_{\text{Edd}} = L_{\text{Bol}}/L_{\text{Edd}}$, the ratio of the quasars’ bolometric to Eddington luminosity.

The quasars’ bolometric luminosities have been estimated from their rest-frame 3000\AA luminosities using the conversion $L_{\text{Bol}} = 5.15 \times \lambda L_{3000}$ ([Shen et al. 2011](#)). [Pons et al. \(2019\)](#) calculated $L_{\text{Bol}} = (1.89 \pm 0.07) \times 10^{47} \text{ erg s}^{-1}$ for DELS J0411–0907, and [Reed et al. \(2019\)](#) calculated $L_{\text{Bol}} = (1.35 \pm 0.03) \times 10^{47} \text{ erg s}^{-1}$ for VDES J0020–3653.

The Eddington luminosity, the theoretical maximum luminosity an object could have while balancing radiation pressure and gravity, is typically assumed to be

$$L_{\text{Edd}} = \frac{4\pi G m_p c M_{\text{BH}}}{\sigma_T} = 1.26 \times 10^{38} \left(\frac{M_{\text{BH}}}{M_\odot} \right) \text{ erg s}^{-1}, \quad (6)$$

where G is the gravitational constant, m_p the proton mass, c the speed of light, and σ_T the Thomson scattering cross-section. Using the various black hole mass estimates from Sect. 3.1.2, we calculated the corresponding Eddington ratios which are listed in Table 2.

From our best estimate of the black hole mass for DELS J0411–0907, $M_{\text{BH}} = (1.85^{+2}_{-0.8}) \times 10^9 M_\odot$, we estimated an

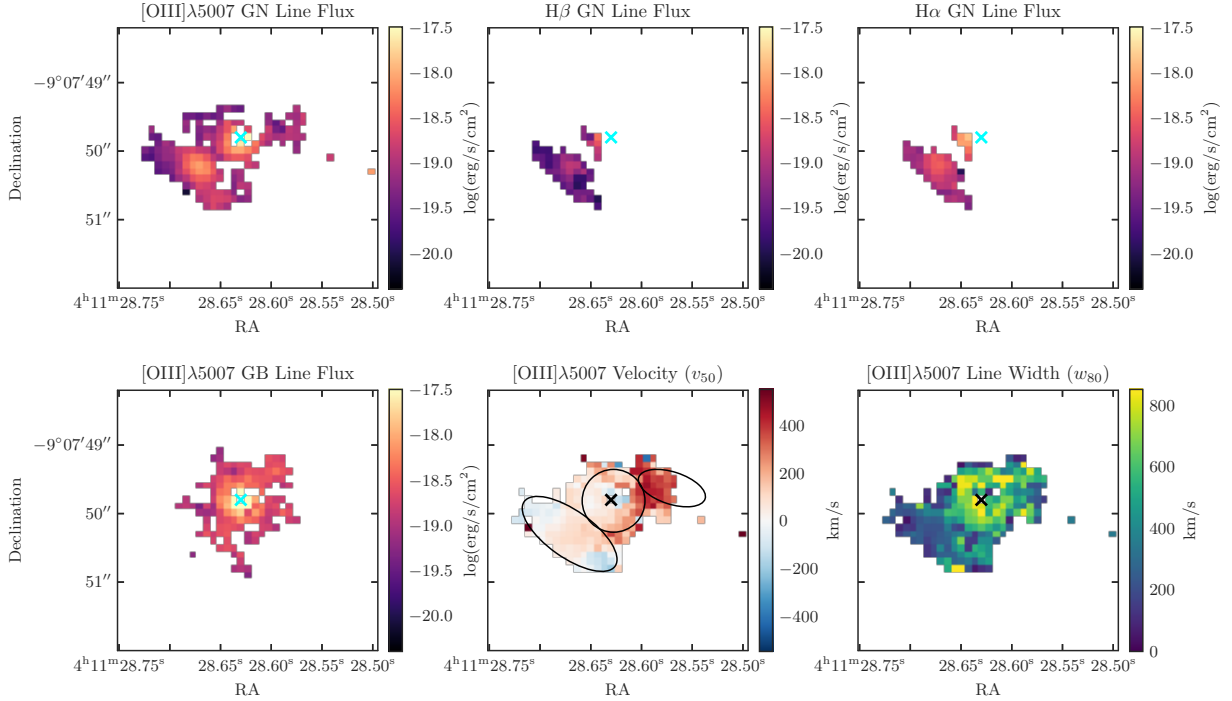


Fig. 4. Flux and kinematic maps for DELS J0411–0907, after the subtraction of the quasar emission using the N&B subtraction technique. The top panels show the flux of the narrow component of the [O III] $\lambda 5007$, H β , and H α lines (GN), as fit by a Gaussian. The bottom left panel shows the flux of the broader GB component of the [O III] $\lambda 5007$ line, a second Gaussian with a larger σ . The lower middle and right panels show our kinematic maps, showing the non-parametric central velocity of the line (v_{50} ; middle) and the line width (w_{80} ; right). As these are non-parametric, this combines both the GN and GB components. We describe our method for creating these maps in Sect. 2.3.4. The black ellipses in the lower middle panel depict the regions as in Fig. 5.

Eddington ratio of $\lambda_{\text{Edd}} = 0.8^{+0.7}_{-0.4}$, with our full range of estimates from 0.6–1.6. In comparison, the Pons et al. (2019) estimate of λ_{Edd} based on Mg II black hole mass is $\lambda_{\text{Edd, Mg II}} = 2.37 \pm 0.22$ for DELS J0411–0907, including only measurement uncertainties and not the scatter in the Mg II black hole mass relation. As discussed in Sect. 3.1.2, instead re-deriving the Mg II black hole mass from the Pons et al. (2019) measurements using the Shen et al. (2011) relation, we calculated $\lambda_{\text{Edd, Mg II}} = 1.6$. With independent spectra, Yang et al. (2021) calculated $\lambda_{\text{Edd, Mg II}} = 1.3 \pm 0.2$, again including only measurement uncertainties.

These Mg II-derived ratios are all above the Eddington limit, with the Pons et al. (2019) measurement implying an extremely rapidly accreting quasar. However, our measurements show that the Eddington ratio is $\lambda_{\text{Edd}} = 0.8^{+0.7}_{-0.4}$, a more moderate accretion rate. In summary, our results indicate that for DELS J0411–0907 the Mg II measurements underestimate the black hole mass, and thus overestimate the accretion rate of the black hole.

VDES J0020–3653 has a lower bolometric luminosity than DELS J0411–0907, and a larger black hole mass, resulting in a lower Eddington ratio for this quasar. From our best estimate of the black hole mass for VDES J0020–3653, $M_{\text{BH}} = (2.9^{+3.5}_{-1.3}) \times 10^9 M_{\odot}$, we estimated an Eddington ratio of $\lambda_{\text{Edd}} = 0.4^{+0.3}_{-0.2}$, with our full range of estimates from 0.2–0.5, except for the large H α estimate of $0.9^{+0.6}$, which could be affected by its proximity to the edge of the detector. In comparison, the estimate of λ_{Edd} based on the Mg II black hole mass was $\lambda_{\text{Edd, Mg II}} = 0.62 \pm 0.12$ for VDES J0020–3653 (Reed et al. 2019), or alternatively $\lambda_{\text{Edd, Mg II}} = 0.43$ as re-calculated by Farina et al. (2022). Our derived Eddington ratios are consistent with both values, which all suggest a sub-Eddington accretion rate for this quasar.

3.2. Host galaxy properties

3.2.1. ISM structure and kinematics

In this section we study the spatial structure of the emission line regions present within our data cubes. To verify the spatial structures that we saw, we produced a second set of data cubes by sub-sampling to a pixel scale of $0.05''/\text{pix}$, and combining the various dithers with a different weighting scheme (see Appendix C), giving higher spatial resolution data cubes. Unfortunately, due to PSF effects the quasar subtraction does not produce successful results using these cubes. As a result, we only used these cubes to qualitatively examine the spatial morphologies in greater detail, with all quantitative results instead using the $0.1''/\text{pix}$ cubes. We show the [O III] $\lambda 5007$ maps, as measured from these $0.05''/\text{pix}$ data cubes in Fig. C.1, and discuss this further in Appendix C.

DELS J0411–0907. Our quasar-subtracted cube for DELS J0411–0907 reveals three extended narrow-line emission regions, as shown in Fig. 5 and labelled as Regions 1, 2, and 3. These three structures can be seen in both the $0.1''/\text{pix}$ and $0.05''/\text{pix}$ cubes. The integrated spectra for each of the regions are also shown in Fig. 5. Our kinematic maps for the subtracted cube, showing the flux of the lines, their relative velocity, and linewidth in each spaxel are shown in Fig. 4 for the N&B quasar subtraction and in Fig. B.1 for the BLR quasar subtraction. We fit the emission lines in the integrated spectra of each of the three regions with either one or two Gaussians, depending on whether a broader wing component was seen, using the spectral fitting method used to construct our kinematic maps described in Sect. 2.3.4. For Region 2, we excluded the central nine pixels surrounding the quasar peak, as these are highly corrupted by the quasar subtraction and

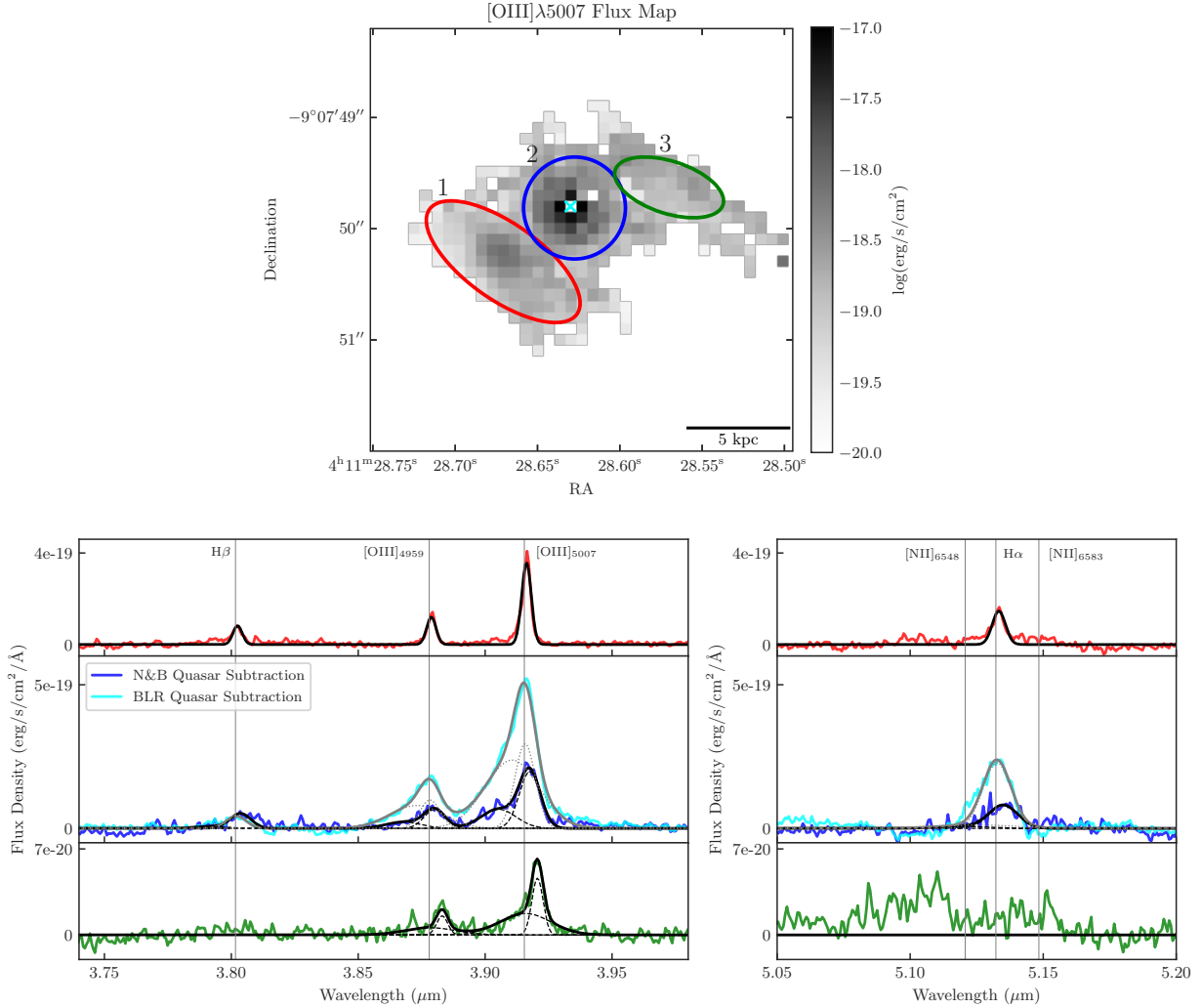


Fig. 5. Emission line regions surrounding DELS J0411–0907. Top: the [O III] $\lambda 5007$ flux map for DELS J0411–0907 after N&B quasar subtraction, with three regions of interest marked. Bottom: the integrated spectrum for the three regions (coloured lines), along with our best fit model in black. The middle panel, for Region 2, also shows the integrated spectra from the BLR quasar subtraction, in cyan, with the best fit model in grey. This region is the host of the quasar (position marked as a cyan cross in the top panel), and so the residual spectrum in this region depends heavily on the type of quasar subtraction. For Regions 1 and 3 the spectrum for both subtraction methods look equivalent, and so the BLR-subtracted spectra are not shown. For Region 2, we exclude the central nine pixels surrounding the quasar peak, as these are highly corrupted by the quasar subtraction and introduce significant noise and artefacts. This means that we slightly underestimate the total flux in this region; however, the fluxes are significantly more reliable than if these nine most corrupted spaxels were included. In Region 1, the spectral lines can be described by a single narrow Gaussian (GN), whereas in Regions 2 and 3 there is also a broader component fit with a second Gaussian (GB); these separate components can be seen as the dashed black lines for the N&B quasar subtraction, and dotted grey lines for the BLR quasar subtraction.

introduce significant noise and artefacts. The extracted flux values and velocities are given in Table 3 and the flux ratios and our derived physical properties are listed in Table 4.

Region 1 is a companion galaxy to the south-east of the quasar. The ellipse defining this region in Fig. 5 is offset $0.78''$ from the quasar position. In WMAP9 cosmology at $z = 6.818$, $1'' = 5.446$ kpc, and so this offset is 4.26 kpc, quasar-to-centre. For reference, the region ellipse, which we fit by eye, has $a = 0.814'' = 4.4$ kpc, $b = 0.341'' = 1.9$ kpc and a PA of 54.6° . By fitting a 2D Gaussian to the spatial distribution of the [O III] $\lambda 5007$ flux in this region, we found that this region can be best described with a $\sigma_a = (0.173 \pm 0.007)'' = 0.94 \pm 0.04$ kpc, an axis ratio of 0.70 ± 0.04 , and a PA of $54 \pm 4^\circ$. We note that this is an unconvolved Gaussian fit to the observed shape, we have not considered the PSF extent or shape to determine an intrinsic size.

From the integrated spectrum, this region has a relative velocity shift of $+65 \pm 51$ km s $^{-1}$ with respect to the quasar's peak [O III] $\lambda 5007$ emission at $z = 6.818$. The GN H β , [O III] $\lambda \lambda 4959, 5007$, and H α lines are all detected with a peak $S/N > 5$, with a line σ of 135 ± 51 km s $^{-1}$. This region does not contain significant GB flux, with the lines well-fit by a single narrow Gaussian component. Considering instead the cube where only the BLR component of the quasar has been subtracted, the [O III] $\lambda \lambda 4959, 5007$ properties of Region 1 are relatively unaffected, while the H β and H α fluxes slightly differ; these values are also given in Tables 3 and 4. This region is spatially offset from the quasar such that narrow flux from the central spaxel, smeared by the PSF, does not contribute strongly. However, some quasar flux is present, hence the slightly different results for the different quasar subtractions.

Table 3. Fluxes and velocities for the $H\alpha$, $H\beta$ and $[O\text{ III}] \lambda\lambda 4959, 5007$ galaxy line components, from the integrated spectra over the regions shown in Figs. 5 and 7 for DELS J0411–0907 (upper panels) and VDES J0020–3653 (lower panels).

	$F_{H\beta}$	$F_{[O\text{ III}]\lambda 4959}$	$F_{[O\text{ III}]\lambda 5007}$	$F_{H\alpha}$	$F_{[N\text{ II}]\lambda 6584}$	V_r	V_σ
		$(10^{-18} \text{ erg s}^{-1} \text{ cm}^{-2}) [S/N]$				(km s^{-1})	(km s^{-1})
DELS J0411–0907							
N&B quasar subtraction							
Region 1, GN	3.8±0.2 [23]	5.6±0.2 [34]	16.8±0.2 [92.4]	9.0±0.4 [21]	<1.0	65±51	135±51
Region 2, GN	5.2±1.1 [4.8]	6.8±0.9 [7.2]	20.5±1.1 [19]	11.0±2.3 [4.7]	<5.1	163±51	314±51
Region 2, GB	<5.5	3.8±1.6 [2.5]	11.6±1.7 [6.8]	<8.6	<8.5	−783±51	526±51
Region 3, GN	<0.4	0.8±0.1 [6.7]	2.5±0.1 [18]	<0.8	<0.8	396±51	161±51
Region 3, GB	<1.9	1.5±0.6 [2.4]	4.4±0.6 [6.8]	<3.5	<3.5	38±51	764±51
BLR quasar subtraction							
Region 1, GN	3.4±0.2 [20]	5.6±0.2 [34]	16.9±0.2 [92.9]	9.4±0.4 [22]	<1.0	64±51	135±51
Region 2, GN	4.2±1.0 [4.1]	9.8±0.9 [11]	29.6±1.0 [28.7]	30.1±2.3 [13]	<4.9	22±51	303±51
Region 2, GB	<8.2	20.9±2.4 [8.8]	62.8±2.5 [25]	<12.6	<12.6	−374±51	807±51
Region 3, GN	<0.4	0.8±0.1 [6.6]	2.5±0.1 [18]	<0.8	<0.8	392±51	162±51
Region 3, GB	<1.9	1.6±0.6 [2.7]	5.0±0.6 [7.6]	<3.5	<3.5	7±51	764±51
VDES J0020–3653							
N&B quasar subtraction							
Region 1, GN	2.1±0.2 [11]	5.4±0.2 [27]	16.2±0.3 [82]	7.9±0.6 [22]	<1.4	−30±51	319±51
Region 2, GN	2.3±1.2 [2.6]	4.8±1.0 [5.3]	14.4±1.0 [16]	17.4±2.8 [11]	<5.9	149±51	369±51
Region 2, GB	<6.7	2.4±1.9 [1.4]	7.4±1.9 [4.3]	<11.5	<11.2	−877±51	698±51
Region 3, GN	1.2±0.2 [8.9]	1.5±0.2 [11]	4.6±0.2 [33]	5.7±0.5 [19]	<1.1	232±51	250±51
Region 4, GN	1.4±0.2 [13]	2.1±0.2 [19]	6.2±0.2 [56]	5.6±0.4 [21]	<0.9	367±51	189±51
BLR quasar subtraction							
Region 1, GN	2.9±0.3 [11]	5.8±0.3 [23]	17.3±0.3 [63]	8.3±0.7 [12]	<1.4	−40±51	332±51
Region 2, GN	4.5±0.9 [5.2]	4.6±0.7 [6.5]	13.7±0.7 [19]	17.9±2.1 [8.5]	<4.0	15±51	263±51
Region 2, GB	16.0±2.9 [5.6]	14.3±2.6 [5.6]	43.1±2.6 [17]	<14.8	<14.6	−460±51	942±51
Region 3, GN	1.3±0.2 [6.1]	1.5±0.2 [7.8]	4.6±0.2 [23]	5.7±0.5 [12]	<1.1	227±51	252±51
Region 4, GN	1.4±0.2 [8.6]	2.1±0.2 [12]	6.2±0.2 [34]	5.6±0.4 [14]	<0.9	367±51	189±51

Notes. The values in braces give the integrated S/N of each line. We present the results from both the N&B quasar subtraction and the BLR quasar subtraction. We fit the narrow line spectra with two components, a true narrow line (GN) as well as a galaxy ‘broad’ wing (GB) component likely associated with outflows; we note that this ‘broad’ component is not from the quasar BLR, which has been subtracted from these spectra. In regions where no broader GB line component is detected, we fit only a single GN component. Upper limits for undetected lines are 3σ limits on the line flux, taken from the ERR array. Uncertainties on the velocity and velocity dispersion assume an uncertainty of ± 1 wavelength element, $\pm 6.65 \text{ \AA}$ or 51 km s^{-1} . The velocity dispersions have been corrected for an instrumental broadening of $\text{FWHM}_{\text{inst}} = 115 \text{ km s}^{-1}$.

Region 2 is the host galaxy of the quasar. The circle defining this region in Fig. 5 has a radius $r = 0.458''$ or 2.5 kpc, for reference. By fitting a 2D Gaussian to the spatial distribution of the $[O\text{ III}] \lambda 5007$ flux in this region, we found that this can be best described with a $\sigma_a = 0.14 \pm 0.02'' = 0.75 \pm 0.09 \text{ kpc}$, an axis ratio of 0.81 ± 0.14 , and a PA of $83 \pm 20^\circ$. The GN $H\beta$, $[O\text{ III}] \lambda\lambda 4959, 5007$, and $H\alpha$ lines are detected with a $S/N \geq 17$, while the brighter $[O\text{ III}] \lambda\lambda 4959, 5007$ lines also exhibit a broader (GB) wing, detected with $S/N \geq 9$. The GN line is offset from the quasar at $z = 6.818$ by $+163 \pm 51 \text{ km s}^{-1}$, with a line σ of $314 \pm 51 \text{ km s}^{-1}$, while the broader wing is offset by $-783 \pm 51 \text{ km s}^{-1}$ with a line σ of $526 \pm 51 \text{ km s}^{-1}$.

These line properties for Region 2 vary significantly when considering the BLR quasar subtracted cube, that has removed only the BLR model of the quasar, instead of the N&B quasar subtracted cube, in which unresolved NLR flux from the centre of the galaxy is also removed. The line properties for the BLR subtracted cube are presented in Table 3, alongside the N&B subtracted properties. The integrated spectrum of this region is also shown for the BLR-subtracted cube in Fig. 5, and clearly contains significantly more flux than for the N&B quasar subtracted cube. This central region is coincident with the quasar, and so this BLR subtracted cube contains the unresolved narrow

line flux from the NLR surrounding the quasar, spread across the image according to the PSF shape. This can also be seen in the flux maps for this BLR-subtracted cube, presented in Fig. B.1, which show the bright central narrow line emission. In the BLR-subtracted cube there is significant GB flux, offset by $-374 \pm 51 \text{ km s}^{-1}$ from the quasar’s GN $[O\text{ III}] \lambda 5007$ peak, with a line σ of $807 \pm 51 \text{ km s}^{-1}$.

Region 3 sits to the north-west of the quasar. The ellipse we fit by eye to define this region in Fig. 5 is offset $0.90'' = 4.9 \text{ kpc}$ from the quasar centre-to-centre, with $a = 0.509'' = 2.8 \text{ kpc}$, $b = 0.235'' = 1.3 \text{ kpc}$ and a PA of 72.1° . This region is not well fit by a 2D Gaussian, so we did not constrain its σ and axis ratio as for the other regions. From the integrated spectrum of this region there are significant detections of $[O\text{ III}] \lambda\lambda 4959, 5007$ GN components and a broader $[O\text{ III}] \lambda 5007$ GB component, with a marginal detection of an $[O\text{ III}] \lambda 4959$ GB component. No $H\alpha$ or $H\beta$ is significantly detected. The GN line component is offset from the quasar at $z = 6.818$ by $+396 \pm 51 \text{ km s}^{-1}$, with a line σ of $161 \pm 51 \text{ km s}^{-1}$, while the broader GB wing is offset by $+38 \pm 51 \text{ km s}^{-1}$ with a line σ of $764 \pm 51 \text{ km s}^{-1}$. With its larger relative velocity and line width, and non-Gaussian spatial distribution, Region 3 is likely a tidal tail. As for Region 1, the BLR subtracted cube produces consistent results to the N&B

Table 4. Flux ratios, SFRs, dust properties, and dust-corrected SFRs for the emission-line regions in DELS J0411–0907 (upper rows) and VDES J0020–3653 (lower rows).

	$\frac{F_{H\alpha}}{F_{H\beta}}$	$\frac{F_{[OIII]\lambda 5007}}{F_{H\beta}}$	$\frac{F_{[NII]\lambda 6584}}{F_{H\alpha}}$	SFR ($M_{\odot} \text{ yr}^{-1}$)	$E(B - V)$ (mag)	$A_{H\alpha}$ (mag)	SFR _{dust corr} ($M_{\odot} \text{ yr}^{-1}$)
DELS J0411–0907							
N&B quasar subtraction							
Region 1, GN	2.4±0.2	4.5±0.2	<0.1	27±1			
Region 2, GN	2.1±0.6	4.0±0.9	<0.5	<33±7			
Region 2, GB	–	>2.1	–				
Region 3, GN	–	>6.3	–				
Region 3, GB	–	>2.4	–				
BLR quasar subtraction							
Region 1, GN	2.8±0.2	5.0±0.2	<0.1	29±1			
Region 2, GN	7.1±1.8	7.0±1.7	<0.2	<91±7			
Region 2, GB	–	>7.6	–				
Region 3, GN	–	>6.3	–				
Region 3, GB	–	>2.7	–				
VDES J0020–3653							
N&B quasar subtraction							
Region 1, GN	3.8±0.5	7.7±0.9	<0.2	24±2	0.2±0.1	0.8±0.4	51 ⁺⁵⁰ _{–22}
Region 2, GN	7.5±3.9	6.2±3.1	<0.3	<54±9			
Region 2, GB	–	>1.1	–				
Region 3, GN	4.8±0.9	3.9±0.7	<0.2	18±2	0.4 ±0.2	1.5 ^{+0.5} _{–0.6}	70 ⁺¹¹⁸ _{–40}
Region 4, GN	4.0±0.5	4.4±0.5	<0.2	17±1	0.3 ±0.1	1.0 ^{+0.4} _{–0.4}	42 ⁺⁴² _{–18}
BLR quasar subtraction							
Region 1, GN	2.9±0.3	6.0±0.5	<0.2	26±2	0.0±0.1	0.0±0.3	27 ⁺¹⁵ _{–8}
Region 2, GN	3.9±0.9	3.0±0.6	<0.3	<55±6			
Region 2, GB	<0.9	2.7±0.5	–				
Region 3, GN	4.6±0.8	3.7±0.6	<0.2	18±2	0.4 ±0.1	1.3 ^{+0.5} _{–0.6}	60 ⁺⁹¹ _{–33}
Region 4, GN	4.0±0.5	4.4±0.5	<0.2	17±1	0.3 ±0.1	1.0 ^{+0.4} _{–0.4}	42 ⁺⁴² _{–18}

Notes. The upper section lists the derived values from the N&B quasar subtraction, and the lower section lists the values from the BLR quasar subtraction. Line ratios are quoted as values if both lines are detected, limits if one line is detected, and not quoted if neither are detected. We note that we constrained $F_{[OIII]\lambda 5007}/F_{[OIII]\lambda 4959} = 3$ in all regions. The uncertainties on SFR consider only the flux measurement uncertainty, and no systematic uncertainty introduced by the conversion Eq. (7). We quote the Region 2 SFR values as upper limits as the AGN photoionisation will contribute, however these are calculated from a measured $H\alpha$ flux, not a $H\alpha$ limit, hence the quoted uncertainties on those values.

quasar-subtracted cube in this region, as Region 3 is spatially offset enough that the narrow-line flux from the quasar has negligible contribution.

VDES J0020–3653. Our quasar-subtracted cube for VDES J0020–3653 also reveals three extended narrow-line emission regions, with their [O III] $\lambda 5007$ flux and integrated spectra shown in Fig. 7. The [O III] $\lambda 5007$ maps made using the higher spatial resolution 0.05"/pix cubes (Fig. C.1) expose a fourth emission line region, separated by only $\sim 0.37''$ or 2 kpc (quasar peak to companion peak) to the south-south-west of the quasar. This is so close to the quasar host that in the 0.1"/pix cubes this appears to be one elongated host galaxy. Using the spatial structure from the higher resolution cube, we defined four region ellipses from which we extracted the spectra in each region. Thus, while the 0.1"/pix cubes can barely distinguish the host and this nearby companion galaxy, using the additional spatial information from the higher resolution cubes we were able to more accurately measure the host galaxy properties from the 0.1"/pix cubes, excluding the additional flux from the nearby companion. The extracted flux values from each of the four region ellipses are given in Table 3, with their flux ratios and derived physical properties in Table 4. Our kinematic maps for

the subtracted cube, showing the flux of the lines, their relative velocity, and linewidth in each spaxel are shown in Fig. 6 for the N&B quasar subtraction and Fig. B.1 for the BLR quasar subtraction.

Region 1 is a companion galaxy to the south-south-west of the quasar, with such a small separation that it is barely resolvable in the 0.1"/pix cube. The ellipse defining this region in Fig. 7 is offset 0.52'' from the quasar position. In WMAP9 cosmology at $z = 6.854$, $1'' = 5.429$ kpc, and so this offset is 2.8 kpc, quasar-to-centre. The ellipse has $a = 0.338'' = 1.8$ kpc, $b = 0.228'' = 1.2$ kpc and a PA of 109° . As this region is blended with the host emission at this small separation, the emission does not follow a 2D Gaussian profile and so we did not quote the best fitting parameters as for the other regions. From the integrated spectrum, this region has a relative velocity shift of $-30 \pm 51 \text{ km s}^{-1}$ with respect to the quasar's peak [O III] $\lambda 5007$ emission at $z = 6.854$. The GN $H\beta$, [O III] $\lambda 4959$, 5007, and $H\alpha$ lines are all detected with a $S/N \geq 11$, with a line σ of $319 \pm 51 \text{ km s}^{-1}$. These lines are well-fit by a single Gaussian component, with no secondary GB flux detected. When using the BLR subtracted cube, the flux is measured to be slightly larger due to contamination by the narrow-line flux from the quasar at this separation. The flux seen around

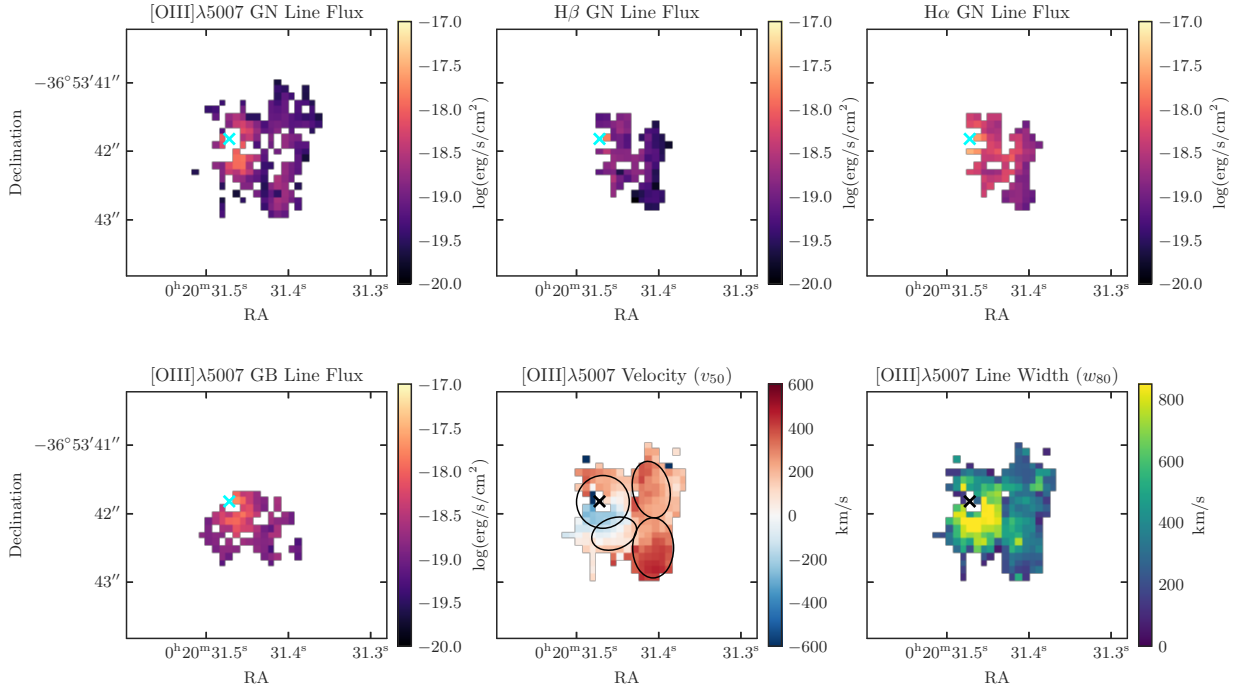


Fig. 6. Kinematic maps for VDES J0020–3653, after the subtraction of the quasar emission using the N&B subtraction technique. The top panels show the flux of the narrow component of the [O III] λ 5007, H β , and H α lines (GN), as fit by a Gaussian. The bottom left panel shows the flux of the broader GB component of the [O III] λ 5007 line, a second Gaussian with a larger σ . The lower middle and right panels show our kinematic maps, showing the non-parametric central velocity of the line (v_{50} ; middle) and the line width (w_{80} ; right). As these are non-parametric, this combines both the GN and GB components. We describe our method for creating these maps in Sect. 2.3.4. The black ellipses in the lower middle panel depict the regions as in Fig. 7.

[N II] λ 6583 in Region 1 is likely remaining broad H α flux from the quasar.

Region 2 is the host galaxy of the quasar. For reference, the circle defining this region in Fig. 7 has a radius $r = 0.385'' = 2.1$ kpc. By fitting a 2D Gaussian to the spatial distribution of the [O III] λ 5007 flux in this region, we found that this can be best described with a $\sigma_a = (0.18 \pm 0.02)'' = (1.0 \pm 0.1)$ kpc, an axis ratio of 0.66 ± 0.12 , and a PA of $26 \pm 10^\circ$. The GN [O III] λ 4959, 5007, H β and H α lines are detected with a $S/N \geq 2.6$. The brighter [O III] λ 4959, 5007 lines also exhibit a broader (GB) wing, detected with $S/N \geq 1.4$. The GN line is offset from the quasar at $z = 6.854$ by $+149 \pm 51$ km s $^{-1}$, with a line σ of 369 ± 51 km s $^{-1}$, while the broader wing is offset by -877 ± 51 km s $^{-1}$ with a large line σ of 698 ± 51 km s $^{-1}$.

As for the host region in DELS J0411–0907, the VDES J0020–3653 line properties for Region 2 vary significantly when considering the BLR quasar subtracted cube. The line properties for the BLR subtracted cube are presented in Table 3, alongside the N&B subtracted properties, and the integrated spectrum for Region 2 for the BLR subtraction is also shown in Fig. 7. As for DELS J0411–0907, this central region is coincident with the quasar, and so this BLR subtracted cube contains the unresolved narrow line flux from the NLR surrounding the quasar, spread across the image according to the PSF shape. This can also be seen in the kinematic maps for this cube, presented in Figs. 6 and B.1, which show the bright central emission.

Region 3 is likely a second companion galaxy to the north-west of the quasar. The ellipse defining this region in Fig. 7 is offset $0.77'' = 4.17$ kpc from the quasar centre-to-centre, with $a = 0.417'' = 2.3$ kpc, $b = 0.271'' = 1.5$ kpc and a PA of

11° . By fitting a 2D Gaussian to the spatial distribution of the [O III] λ 5007 flux in this region, we found that this can be best described with a $\sigma_a = (0.4 \pm 0.1)'' = (2.0 \pm 0.5)$ kpc, an axis ratio of 0.6 ± 0.2 , and a PA of $193 \pm 5^\circ$. In this region there are significant detections of GN [O III] λ 4959, 5007, H β and H α components, with $S/N \geq 8.9$. The GN line component is offset from the quasar at $z = 6.854$ by $+232 \pm 51$ km s $^{-1}$, with a line σ of 250 ± 51 km s $^{-1}$. No broader GB component is detected. The properties of Region 3 are relatively unaffected when considering instead the BLR quasar subtracted cube; these are also given in Tables 3 and 4. This region is spatially offset from the quasar such that no significant narrow flux from the central region contributes.

Region 4 is a companion galaxy to the south-west of the quasar. The ellipse defining this region in Fig. 7 is offset $1.03'' = 5.61$ kpc from the quasar position, quasar-to-centre. For reference, the region ellipse that we fit by eye has $a = 0.439'' = 2.4$ kpc, $b = 0.299'' = 1.6$ kpc and a PA of 0° . By fitting a 2D Gaussian to the spatial distribution of the [O III] λ 5007 flux in this region, we found that this region can be best described with a $\sigma_a = 0.43 \pm 0.08'' = 2.3 \pm 0.4$ kpc, an axis ratio of 0.47 ± 0.13 , and a PA of $-4 \pm 2^\circ$. We note again that this is an unconvolved Gaussian fit to the observed shape. From the integrated spectrum, this region has a relative velocity shift of $+367 \pm 51$ km s $^{-1}$ with respect to the quasar's peak [O III] λ 5007 emission at $z = 6.854$. The GN H β , [O III] λ 4959, 5007, and H α lines are all detected with a $S/N \geq 13$, with a line σ of 189 ± 51 km s $^{-1}$. These lines are well-fit by a single Gaussian component, with no GB flux detected. As for Region 3, the BLR subtracted cube has consistent results to the N&B quasar-subtracted cube, as Region 4 is spatially offset enough that the narrow-line flux from the quasar has negligible contribution.

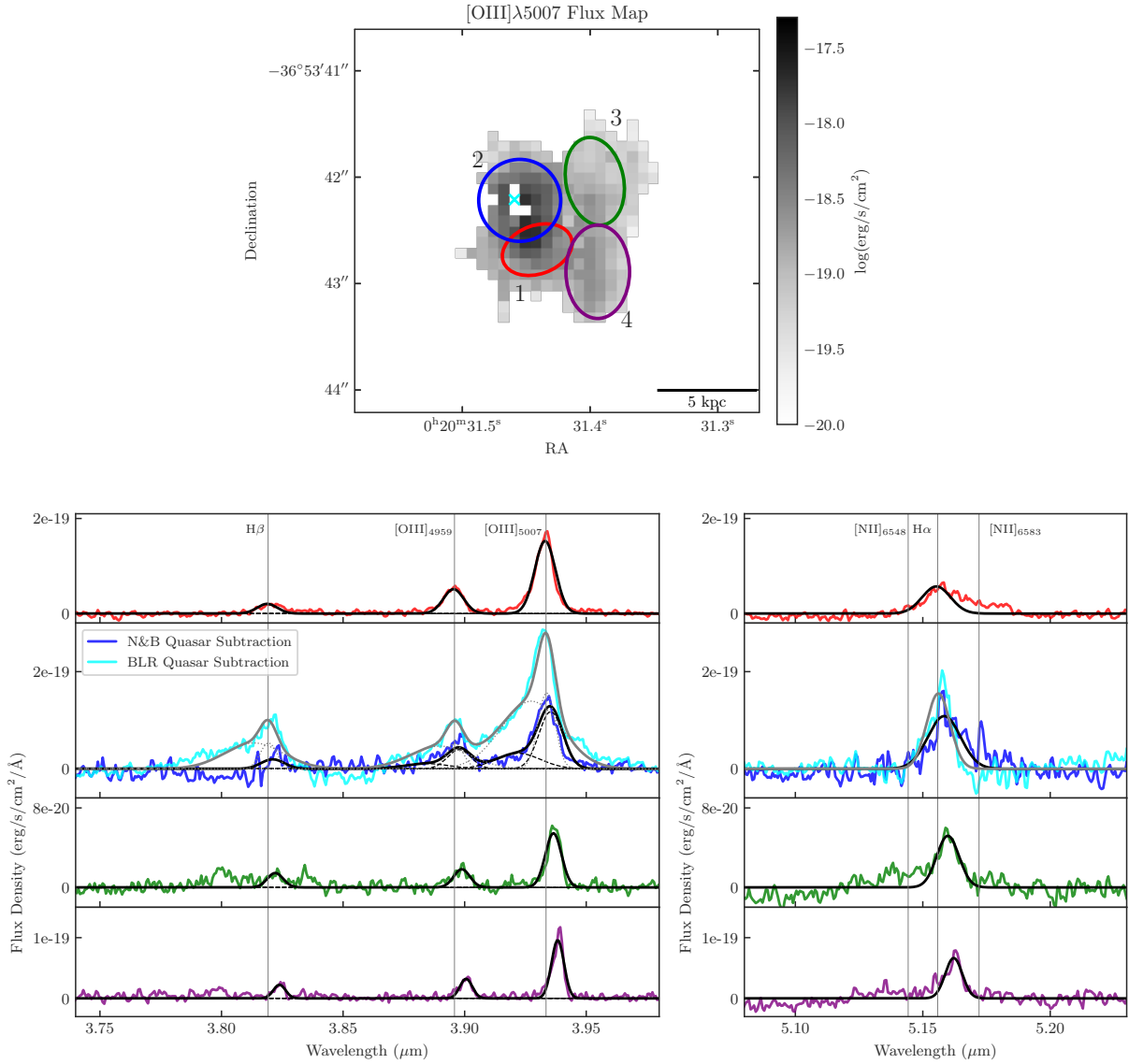


Fig. 7. Emission line regions surrounding VDES J0020–3653. Top: the [O III] $\lambda 5007$ flux map for VDES J0020–3653 after N&B quasar subtraction, with four regions of interest marked. Bottom: the integrated spectrum for the four regions (coloured lines), along with our best fit model in black. The middle panel, for Region 2, also shows the integrated spectra from the BLR quasar subtraction, in cyan, with the best fit model in grey. This region is the host of the quasar (position marked as a cyan cross in the top panel), and so the residual spectrum in this region depends heavily on the type of quasar subtraction. We note that to account for the overlapping area between Regions 1 and 2, we assigned the flux in those spaxels to Region 1 only. For Region 2, we excluded the central nine pixels surrounding the quasar peak, as these are highly corrupted by the quasar subtraction and introduce significant noise and artefacts. This means that we slightly underestimate the total flux in this region, however the fluxes are significantly more reliable than if these nine most corrupted spaxels were included. In Regions 1, 3, and 4, the spectral lines can be described by a single narrow Gaussian (GN), whereas in Region 2 there is also a broader component which we fit with a second Gaussian (GB); these separate components can be seen as the dashed black lines for the N&B quasar subtraction, and dotted grey lines for the BLR quasar subtraction. We note that the emission around $3.8 \mu\text{m}$ in Regions 3 and 4 is likely an artefact in the cube. We did not see any significant detection of [N II] $\lambda\lambda 6548, 6583$.

3.2.2. Limits on star formation rates and excitation mechanisms

Using our integrated spectrum for each region, we estimated the SFR using the GN $H\alpha$ line flux. Assuming no extinction, a solar abundance, and a Salpeter IMF, the SFR can be estimated as:

$$\text{SFR} = 5.37 \times 10^{-42} \frac{L_{H\alpha}}{(\text{erg s}^{-1})} M_{\odot} \text{ yr}^{-1} \quad (7)$$

(Kennicutt & Evans 2012, we note that these values are 68% of those calculated assuming the Kennicutt 1998 relation). We used this equation to calculate the SFR for each of the regions in

which $H\alpha$ is detected. The resulting SFRs for DELS J0411–0907 and VDES J0020–3653 are given in Table 4.

This equation assumes that all of the $H\alpha$ emission is from star formation; for our host galaxies, however, we note that even for our N&B quasar subtracted cubes we expect some AGN-photoionised narrow line flux to contribute. The N&B quasar subtraction removes all of the GN component that is emitted from the central unresolved region surrounding the quasar, although spatially resolved GN flux from both the NLR and star formation remains. Thus, while the N&B quasar subtracted cubes provide the most accurate measurement of the SFRs of our emission-line regions, in comparison to the BLR

subtracted cubes, for our host components these are upper limits. For comparison, we also include the SFRs calculated using the BLR quasar subtracted cube in Table 4, which includes all quasar NLR emission, showing the significant improvement that the narrow-line quasar subtraction can have on being able to measure host galaxy properties. For DELS J0411–0907, the host SFR measured from the N&B subtraction is $<33 M_{\odot} \text{ yr}^{-1}$, whereas the BLR subtraction can only constrain the SFR to $<91 M_{\odot} \text{ yr}^{-1}$, a much larger upper limit. The host galaxy of VDES J0020–3653 has SFR constraints of $<55 M_{\odot} \text{ yr}^{-1}$, consistent for both the BLR and N&B subtractions, likely due to the noisy subtraction around $H\alpha$.

In the absence of dust extinction, theoretically the ratio of $H\alpha$ to $H\beta$ flux is $F_{H\alpha}/F_{H\beta} \approx 2.86$, estimated using a temperature $T = 10^4 \text{ K}$ and an electron density $n_e = 10^2 \text{ cm}^{-3}$ for Case B recombination (Osterbrock 1989; Domínguez et al. 2013). Hence, the amount of dust can be estimated from these two lines via $E(B - V) = 1.97 \log_{10}[(F_{H\alpha}/F_{H\beta})/2.86]$ following Domínguez et al. (2013), and so $A_{H\alpha} = (3.33 \pm 0.80) \times E(B - V)$ assuming the Calzetti et al. (2000) reddening law. For companion regions where both $H\alpha$ and $H\beta$ are significantly detected and $F_{H\alpha}/F_{H\beta} > 2.86$, we calculated $E(B - V)$, $A_{H\alpha}$ and a dust-corrected SFR, which are given in Table 4. As the host regions contain NLR quasar-photoionised flux which can have significantly higher $H\alpha/H\beta$ ratios than the 2.86 assumed here, we did not calculate dust-corrected SFR limits for the host galaxies.

For DELS J0411–0907, the companion galaxy Region 1 has a SFR of $27 \pm 1 M_{\odot} \text{ yr}^{-1}$, as measured from the N&B quasar subtracted spectrum. As the $F_{H\alpha}/F_{H\beta}$ ratio is <2.86 , we did not estimate the dust corrected values. These flux ratios are unlikely to be truly <2.86 , with this more likely being an issue with the quasar subtraction technique and its removal of flux, as the N&B subtraction has $F_{H\alpha}/F_{H\beta} = 2.4 \pm 0.1$ while the BLR subtraction has $F_{H\alpha}/F_{H\beta} = 2.8 \pm 0.1$. The BLR quasar subtraction results in slightly more $H\alpha$ flux, corresponding to a SFR of $29 \pm 1 M_{\odot} \text{ yr}^{-1}$, as well as a lower $H\beta$ flux which also contributes to the larger $F_{H\alpha}/F_{H\beta}$. For this region only, we therefore consider the BLR subtraction to provide the best estimate of the SFR, $29 \pm 1 M_{\odot} \text{ yr}^{-1}$, whereas for all other regions the N&B subtraction provides the best estimate.

For VDES J0020–3653, the companion galaxy Region 1 has a SFR of $24 \pm 2 M_{\odot} \text{ yr}^{-1}$ as measured from the N&B quasar subtracted spectrum, or $51^{+50}_{-22} M_{\odot} \text{ yr}^{-1}$ when corrected for dust attenuation. Using the BLR subtraction, the SFR is similarly $26 \pm 2 M_{\odot} \text{ yr}^{-1}$. However, this subtraction results in a much lower $H\alpha/H\beta$ ratio of 2.91 ± 0.3 , due to contamination from the unresolved quasar emission, and so in this case there is minimal change in the SFR when corrected for dust attenuation, $27^{+15}_{-8} M_{\odot} \text{ yr}^{-1}$. The companion galaxy Region 3 has a SFR of $18 \pm 2 M_{\odot} \text{ yr}^{-1}$, as measured from the N&B quasar subtracted spectrum, or $70^{+118}_{-40} M_{\odot} \text{ yr}^{-1}$ when corrected for dust attenuation, due to its large $H\alpha/H\beta$ ratio. Region 4 has a SFR of $17 \pm 1 M_{\odot} \text{ yr}^{-1}$, as measured from both the N&B quasar subtracted and BLR quasar subtracted spectrum. When corrected for dust-attenuation, this SFR increases to $42^{+42}_{-18} M_{\odot} \text{ yr}^{-1}$. The subtraction method makes little difference for the companion regions 3 and 4, which are sufficiently spatially separated from the quasar such that the unresolved quasar emission has little contribution (see Table 4).

We note that our quasar hosts and companion galaxies have no detected [N II] $\lambda\lambda 6548, 6583$ emission, implying low metallicities. For our SFR calculation we used the typically used conversion from $H\alpha$ in Eq. (7), which is calculated for solar abundances. Lee et al. (2009) recalculated the SFR– $L_{H\alpha}$ relation

for a range of metallicities using the Bruzual & Charlot (2003) population synthesis models. Assuming a case B recombination with nebular temperature of 10^4 K , a density of 100 cm^{-3} , and a Salpeter IMF, Lee et al. (2009) found that the ratio $\text{SFR}/L_{H\alpha}$ in Eq. (7) decreases from 7.9×10^{-42} at $Z = Z_{\odot}$, to 6.2×10^{-42} at $Z = 0.2 Z_{\odot}$ and 5.2×10^{-42} at $Z = 0.02 Z_{\odot}$. This would reduce our calculated SFRs by 22% and 34%, respectively.

We did not detect any [N II] $\lambda\lambda 6548, 6583$ emission from our quasars, their hosts or their companions. To place upper limits on the amount of [N II] $\lambda 6583$ present in the different emission-line regions, we integrated the ERR array at the expected location of the line, assuming a line width equal to that of [O III] $\lambda 5007$. Our [N II] $\lambda 6583$ limits are given in Table 3, with the resulting [N II] $\lambda 6583/H\alpha$ flux ratio limits in Table 4.

Using our measured flux values and limits, we were able to place our emission line regions on a BPT diagram (Baldwin et al. 1981), which we show in Fig. 8. We only considered regions where both the $H\alpha$ and $H\beta$ lines are significantly detected (see Table 4). This diagnostic aims to characterise the main photoionisation source based on the narrow line flux. For this we used the BLR quasar subtracted cube, as this gives the purest measure of the full narrow line flux, whereas in the N&B subtraction a large portion of the quasar NLR flux has been removed.

We found that for both quasars, the companion emission regions (Region 1 for DELS J0411–0907 and Regions 1, 3 and 4 for VDES J0020–3653) have $\log(F_{[\text{O III}]\lambda 5007}/F_{H\beta})$ between 0.55 and 0.78. DELS J0411–0907 Region 1 lies within the region of the diagram typically populated by galaxies that are primarily ionised by star formation. The VDES J0020–3653 companion regions could lie in the star-forming regime or in the transition region, and Region 1 could also lie within the AGN regime, depending on the ratio $F_{[\text{N II}]\lambda 6584 \text{ \AA}}/F_{H\alpha}$, for which we only have upper limits due to a lack of [N II] $\lambda 6583$ detected in our sources.

The quasar host galaxies (Region 2) have $\log(F_{[\text{O III}]\lambda 5007}/F_{H\beta}) = 0.85$ and 0.48 for DELS J0411–0907 and VDES J0020–3653, with $\log(F_{[\text{N II}]\lambda 6584 \text{ \AA}}/F_{H\alpha}) < -0.77$ and -0.48 . For DELS J0411–0907 we found that the host lies in the upper left of the diagram, which is sparsely populated by low- z objects, although lies within the AGN-dominated regime according to the low- z Kewley et al. (2001) demarcation. For VDES J0020–3653, the quasar host lies within the low- z transition region or star-forming regime. Theoretical models predict that high- z AGN will reside in the left side of the BPT diagram, in the AGN regime that is sparsely populated at $z = 0$ as well in the star-forming regime, mainly due to their lower metallicities (see e.g. Feltre et al. 2016; Strom et al. 2017; Nakajima & Maiolino 2022; Hirschmann et al. 2023). This is consistent with our measurements for both quasar host galaxies. For further discussion on this topic, see Übler et al. (2023).

To accurately determine the primary photoionisation mechanism within these various regions, we would require either deeper observations for a [N II] $\lambda 6583$ detection or tighter limit, or alternative line-ratio diagnostic methods. We could use a [S II] $\lambda\lambda 6717, 6731$ -based diagnostic (e.g. Veilleux & Osterbrock 1987); however, [S II] $\lambda\lambda 6717, 6731$ emission was not detected for these quasars. For the integrated quasar spectrum, by integrating the corresponding ERR array across the expected location of the [S II] $\lambda 6717$ line, assuming the same line width as the narrow $H\alpha$ component (Table 1), and applying our aperture correction, we found $F_{[\text{S II}]\lambda 6717} < 2.8 \times 10^{-18} \text{ erg s}^{-1} \text{ cm}^{-2}$ (3σ) for DELS J0411–0907. For VDES J0020–3653, this line is beyond the wavelength coverage of the detector. These lines are either very close to or just above the detectable wavelength

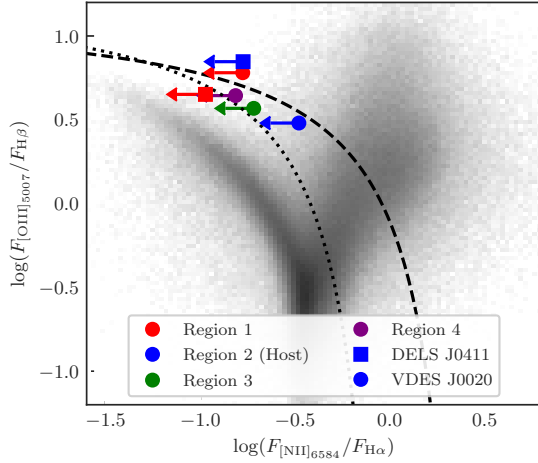


Fig. 8. BPT diagnostic diagram showing the flux ratios of the various emission regions for DELS J0411–0907 (squares) and VDES J0020–3653 (circles); the $F_{[\text{NII}]\lambda 6584}/F_{\text{H}\alpha}$ ratios are all upper limits due to a non-detection of $[\text{NII}]\lambda 6583$. The different colours represent the different emission regions, following the colour scheme in Figs. 5 and 7. The flux ratios were measured from the BLR-subtracted cube. For reference, we show the Kauffmann et al. (2003, black dotted) and Kewley et al. (2001, black dashed) curves which attempt to differentiate between galaxies primarily ionised by star formation (lower left) and AGN (upper right) at low- z . We also show local sources from the SDSS (Abazajian et al. 2009) as the 2D histogram, for comparison.

range for this *G395H/F290LP* NIRSspec configuration, making accurate measurements difficult if a line was detected. We have also not detected any He II $\lambda 4686$ emission, which is particularly useful for distinguishing star formation and AGN dominated regions in the high- z Universe where metallicities are low (see e.g. Nakajima & Maiolino 2022; Übler et al. 2023). For the integrated quasar spectrum, following the same process for $[\text{SII}]\lambda 6717$ but instead assuming the same line width as the narrow $[\text{OIII}]\lambda 5007$ component (Table 1), we found $F_{\text{HeII}\lambda 4686} < 2.3 \times 10^{-18} \text{ erg s}^{-1} \text{ cm}^{-2}$ (3σ) for DELS J0411–0907 and $F_{\text{HeII}\lambda 4686} < 1.6 \times 10^{-18} \text{ erg s}^{-1} \text{ cm}^{-2}$ (3σ) for VDES J0020–3653.

3.2.3. Dynamical masses and black hole–dynamical mass ratios

To calculate the dynamical masses of the various emission regions, we followed the method as in Decarli et al. (2018) for ALMA quasar host studies. Firstly, we assumed that each region is dispersion-dominated, with:

$$M_{\text{dyn,dispersion}} = \frac{3}{2} \frac{R\sigma^2}{G} \quad (8)$$

where R is the radius of the region, σ the integrated line width, and G the gravitational constant. As an alternative, we assumed that the regions are rotation-dominated thin discs, with:

$$M_{\text{dyn,rotation}} = \frac{R}{G} \left(\frac{0.75 \text{ FWHM}}{\sin(i)} \right)^2 \quad (9)$$

where 0.75 FWHM scales the line FWHM to the width of the line at 20% of the peak as in Willott et al. (2015), and i is the inclination angle of the thin disc. Finally, we also considered the virial approximation

$$M_{\text{dyn,virial}} \approx \frac{5R\sigma^2}{G}. \quad (10)$$

This commonly used scaling factor of five was found to be the optimal scaling factor when calibrated to a sample of 25 galaxies by Cappellari et al. (2006; see e.g. van der Wel et al. 2022, for further discussion). This estimate is a factor of 10/3 larger than $M_{\text{dyn,dispersion}}$ by construction. As it is most common for high- z quasar host studies to assume a rotating disc geometry (e.g. Wang et al. 2013; Willott et al. 2015; Decarli et al. 2018), we chose our best dynamical mass estimate to be $M_{\text{dyn,rotation}}$.

To measure the radii, we fit a 2D Gaussian to the spatial distribution of the $[\text{OIII}]\lambda 5007$ emission from each region, and took R to be the σ of the semi-major axis; these values are described in Sect. 3.2.1. From this Gaussian fit we also measured the axis-ratio, b/a , from which we derived the inclination angle, i , via $\cos(i) = b/a$. As above, we note that R and b/a have not been deconvolved by the PSF. For the emission line widths we took the GN $[\text{OIII}]\lambda 5007$ component, which is the brightest of the lines we have measured. We note that this line width represents the total dynamics of the gas, including rotation as well as non-rotational components such as dispersion and winds (see e.g. Wisnioski et al. 2018). We considered only the N&B quasar subtracted cube for this calculation, since otherwise the measurements could be skewed by the unresolved NLR regions around the quasar. The kinematics of this central NLR are not dominated by the larger-scale galaxy potential, thus this emission does not trace the dynamical mass. Considering only the N&B quasar subtracted cube ensures that we are measuring the spatially extended host regions and not the PSF shape, which is particularly important for the host regions (Region 2). The values used in these calculations and the resulting dynamical mass estimates are listed in Table 5.

For DELS J0411–0907, for Region 1 we found a dynamical mass between $0.6\text{--}2.5 \times 10^{10} M_{\odot}$, with a best estimate of $M_{\text{dyn,rotation}} = (2.5^{+3.1}_{-1.6}) \times 10^{10} M_{\odot}$, from an inclination angle $i = 45 \pm 3^{\circ}$. For the host Region 2, we found that the rotational measure for the dynamical mass, $M_{\text{dyn,rotation}} = (16^{+59}_{-9}) \times 10^{10} M_{\odot}$, is larger than the two other estimates, $M_{\text{dyn,dispersion}} = (2.6^{+1.3}_{-1.0}) \times 10^{10} M_{\odot}$ and $M_{\text{dyn,virial}} = (8.6^{+4.4}_{-3.3}) \times 10^{10} M_{\odot}$, albeit with large uncertainties particularly due to the inclination angle, $i = 36^{+12}_{-17}$. This difference is due to our measured inclination angle for this region being relatively low, and so the inclination correction is relatively large. For their ALMA quasar host galaxies that are marginally resolved, and thus where their axis ratio could not be accurately measured, Willott et al. (2015) and Decarli et al. (2018) assumed an inclination of 55° , the median inclination of the resolved sources in Willott et al. (2015) and Wang et al. (2013). As our quasar hosts are difficult to measure, requiring the quasar subtraction, and they are interacting systems which complicates their structure, we are not confident in our inclination measurements. If we instead assumed the median $i = 55^{\circ}$, the rotational dynamical mass is $(8.0^{+4.1}_{-3.0}) \times 10^{10} M_{\odot}$, similar to the virial estimate. For Region 2 of DELS J0411–0907, we therefore assumed a best dynamical mass estimate of $M_{\text{dyn,virial}} = (8.6^{+4.4}_{-3.3}) \times 10^{10} M_{\odot}$. Region 3 cannot be well described by a 2D Gaussian, and so we could not perform our fit as for the other regions.

VDES J0020–3653 Region 1 also cannot be well described by a 2D Gaussian, due to contamination by the quasar host, and so we did not estimate its dynamical mass. For the VDES J0020–3653 host Region 2, we found a dynamical mass between $4.6\text{--}17 \times 10^{10} M_{\odot}$, with a best estimate of $M_{\text{dyn,rotation}} = (17^{+18}_{-8}) \times 10^{10} M_{\odot}$, from an inclination of $i = 49^{+8}_{-10}$. This is similar to the median inclination of the resolved sources in Willott et al. (2015) and Wang et al. (2013), $i = 55^{\circ}$, which would reduce the value

Table 5. Dynamical masses, and values used in their calculation, for the emission-line regions in DELS J0411–0907 (upper rows) and VDES J0020–3653 (lower rows), using the N&B quasar subtraction.

	R (kpc)	σ (km s ⁻¹)	a/b	i (deg)	$M_{\text{dyn,disp}}$ (10 ¹⁰ M_{\odot})	$M_{\text{dyn,rot}}$ (10 ¹⁰ M_{\odot})	$M_{\text{dyn,rot}, i = 55^{\circ}}$ (10 ¹⁰ M_{\odot})	$M_{\text{dyn,vir}}$ (10 ¹⁰ M_{\odot})
DELS J0411–0907								
Region 1, GN	0.94 ± 0.04	135 ± 51	0.70 ± 0.04	45 ± 3	0.6 ^{+0.6} _{-0.4}	2.5 ^{+3.1} _{-1.6}		2.0 ^{+1.9} _{-1.2}
Region 2, GN	0.75 ± 0.09	314 ± 51	0.81 ± 0.14	36 ⁺¹² ₋₁₇	2.6 ^{+1.3} _{-1.0}	16 ⁺⁵⁹ ₋₉	8.0 ^{+4.1} _{-3.0}	8.6 ^{+4.4} _{-3.3}
VDES J0020–3653								
Region 2, GN	0.97 ± 0.13	369 ± 51	0.66 ± 0.12	49 ⁺⁸ ₋₁₀	4.6 ^{+2.1} _{-1.6}	17 ⁺¹⁸ ₋₈	14 ⁺⁷ ₋₅	15 ⁺⁷ ₋₅
Region 3, GN	2.15 ± 0.60	250 ± 51	0.58 ± 0.23	54 ⁺¹⁵ ₋₁₉	4.7 ^{+4.0} _{-2.5}	15 ⁺³⁹ ₋₁₀		16 ⁺¹³ ₋₈
Region 4, GN	2.46 ± 0.51	189 ± 51	0.46 ± 0.14	62 ± 9	3.1 ^{+2.9} _{-1.8}	8.1 ^{+11.2} _{-5.1}		10 ⁺¹⁰ ₋₆

Notes. DELS J0411–0907 Region 3 and VDES J0020–3653 Region 1 cannot be well described by a 2D Gaussian, and so we did not measure their dynamical mass.

slightly to $M_{\text{dyn,rotation}} = (14_{-5}^{+7}) \times 10^{10} M_{\odot}$. Region 3 has dynamical mass estimates of $4.7\text{--}15 \times 10^{10} M_{\odot}$, with our best estimate $M_{\text{dyn,rotation}} = (15_{-10}^{+39}) \times 10^{10} M_{\odot}$ from an inclination of $54_{-19}^{+15^{\circ}}$. For VDES J0020–3653 Region 4 we found a dynamical mass between $3.1\text{--}10 \times 10^{10} M_{\odot}$, with a best estimate from $M_{\text{dyn,rotation}}$ of $(8.1_{-5.1}^{+11.2}) \times 10^{10} M_{\odot}$ with an inclination of $i = 62 \pm 9^{\circ}$.

We plot the dynamical mass–black hole mass relation in Fig. 9 for these two quasars. We found that both of our quasars lie above the local Kormendy & Ho (2013) black hole–stellar mass relation, although these are consistent within the scatter and uncertainties. Previous ALMA observations have found that luminous quasars generally lie above the local black hole–host relation, while lower luminosity quasars lie around or below the relation (see e.g. Willott et al. 2017; Izumi et al. 2019). Our luminous quasars lie above the relation, which is consistent with this existing picture, however a larger sample of high- z quasars is required to test this scenario with NIRSPEC. For a true comparison to the local black hole–stellar mass relation, we require stellar and not dynamical masses.

We note that in the current observations the faint host galaxy continuum emission is not detectable, and so we could not measure their stellar masses. Our high spectral resolution ($R \simeq 2700$) observations were designed to study the emission lines in detail. This sacrifices the sensitivity that is required to detect the host continuum, which is expected to be achievable in similar exposure times at lower spectral resolution (either $R \sim 100$ IFU spectra, or alternatively images as in e.g. Ding et al. 2023; Harikane et al. 2023). Future work within the GA-NIFS GTO programme will use the $R \sim 100$ prism mode to search for the continuum emission of several high- z quasar host galaxies, which would make stellar mass measurements possible.

In Fig. 9 we also find that both of our quasars have dynamical masses and black hole–dynamical mass ratios consistent with ALMA observations of $z \gtrsim 6$ quasars. However, we note that DELS J0411–0907 and VDES J0020–3653 do not have published ALMA dynamical mass estimates that could be used for a direct comparison of these methods for our targets. A detailed comparison of ALMA and JWST NIRSPEC dynamical mass and JWST stellar mass estimates will be a key aim of future quasar studies, which will allow for a much deeper understanding of the high- z black hole–host mass relations.

3.3. Outflow properties

The clear detection of an outflow component, as traced by the broad kinematic component (GB components in Fig. 2) via the

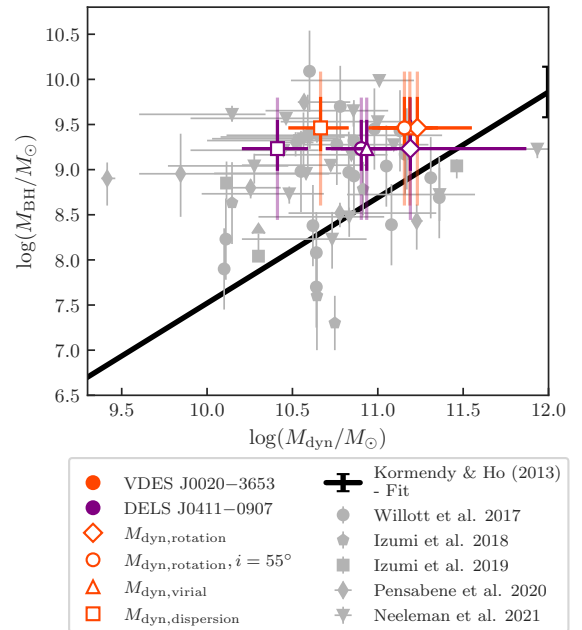


Fig. 9. Dynamical mass–black hole mass relation. Our two quasars DELS J0411–0907 (purple) and VDES J0020–3653 (orange) are shown, with the four M_{dyn} estimates, $M_{\text{dyn,rotation}}$, $M_{\text{dyn,rotation}}$ assuming an inclination angle of 55° , $M_{\text{dyn,dispersion}}$ and $M_{\text{dyn,virial}}$. The solid black hole mass error bars show the 1σ uncertainty on our best estimate of the black hole mass, while the transparent error bars very conservatively show the range of the lower limit of the lowest mass estimate to the upper limit of the largest mass estimate. The black line shows the local Kormendy & Ho (2013) relation. The grey points show a range of observations of high- z quasars as measured via their cold gas from ALMA (Willott et al. 2017; Izumi et al. 2018, 2019; Pensabene et al. 2020; Neeleman et al. 2021).

analysis of the [O III] $\lambda 5007$ velocity and spatial distribution, opens the possibility of investigating the ionised outflow properties in these early quasars. We note that this is the first time that it is possible to properly characterise the ionised outflows in quasars in the Epoch of Reionisation. Previous studies have relied on spatially unresolved information, and in particular on the detection of UV broad and blueshifted absorption features of UV resonant lines (e.g. Wang et al. 2018; Ginolfi et al. 2018; Onoue et al. 2019; Bischetti et al. 2022, 2023). These features trace primarily the nuclear outflow, which is generally a small

Table 6. Properties of the quasar outflows as measured in Sect. 3.3, for DELS J0411–0907 and VDES J0020–3653.

	$L_{H\beta,GB}$	$L_{[OIII],GB}$	v_{out}	R_{out}	$M_{out,H\beta}$	$M_{out,[OIII]}$	$\dot{M}_{out,H\beta}$	$\dot{M}_{out,[OIII]}$	$P_{out,H\beta}$	$P_{out,[OIII]}$
	(10^{43} erg s $^{-1}$)	(10^{43} erg s $^{-1}$)	(km s $^{-1}$)	(kpc)	($10^7 M_{\odot}$)	($10^7 M_{\odot}$)	(M_{\odot} yr $^{-1}$)	(M_{\odot} yr $^{-1}$)	(10^{43} erg s $^{-1}$)	(10^{43} erg s $^{-1}$)
DELS J0411–0907	$1.0^{+0.8}_{-0.7}$	13.5 ± 0.6	1296 ± 31	4.0 ± 0.4	17^{+13}_{-11}	$10.8^{+0.5}_{-0.4}$	58^{+44}_{-37}	$36.2^{+1.9}_{-1.7}$	$3.1^{+2.3}_{-2.0}$	1.9 ± 0.1
VDES J0020–3653	$5.7^{+0.8}_{-1.0}$	$9.6^{+0.5}_{-0.4}$	1749 ± 55	3.3 ± 0.4	97^{+14}_{-17}	$7.7^{+0.4}_{-0.3}$	525^{+75}_{-92}	$41.4^{+2.6}_{-2.2}$	51 ± 9	4.0 ± 0.3

Notes. The luminosities and velocities were taken from the H β and [O III] λ 5007 GB components from the full integrated quasar spectrum (Fig. 2 and Table 1), while the outflow extent R_{out} was measured from the spatial distribution of [O III] λ 5007 where $w_{80} > 600$ km s $^{-1}$, in the BLR-subtracted cube.

fraction of the global, galactic scale outflow, and the lack of spatial information generally prevents a reliable estimate of the outflow parameters such as the outflow rate, kinetic power and momentum rate. We also note that NIRSpc fixed-slit spectroscopic observations of these two quasars covering the rest-frame UV do not reveal any broad absorption features (Willott, priv. comm.), indicating that the presence of ionised outflow is not necessarily traced by broad absorption features in the UV part of the spectrum (see e.g. Rankine et al. 2020).

In this work we have found outflow signatures within H α , H β and [O III] λ 4959, 5007 for both quasars (GB components, Fig. 2). In this section we used the flux, velocity and spatial information of the H β and [O III] λ 5007 broad galaxy (GB) components to infer some of the basic properties of the ionised outflow. We used the GB fluxes and velocities measured from our full integrated spectral fit for the quasar and host galaxy, prior to quasar subtraction, as described in Sect. 2.3.1 and shown in Fig. 2. This gives the most reliable measurements of the integrated quantities, as these are not affected by the quasar subtraction technique. To measure the spatial extent of the outflow, we used the quasar BLR-subtracted cube, from which we can measure the [O III] λ 5007 line width in each spaxel without contamination from the quasar’s BLR. For this we considered the full cube, without splitting the emission into regions as in Sect. 3.2 above. The broad flux emanates from the quasar, approximately covering Region 2 for both quasars, as well as extending into Region 3 for DELS J0411–0907—this can be seen in the w_{80} maps in Fig. B.1.

To derive the mass of the ionised outflow as inferred from the blueshifted ‘outflow’ component of H β , we used the equation

$$M_{out} = 1.7 \times 10^9 C \left(\frac{L_{H\beta}}{10^{44} \text{ erg s}^{-1}} \right) \left(\frac{\langle n_e \rangle}{500 \text{ cm}^{-3}} \right)^{-1} M_{\odot} \quad (11)$$

from Carniani et al. (2015), assuming a density of the gas in the ionised outflow of $\langle n_e \rangle = 500$ cm $^{-3}$, as in Carniani et al. (2015), and where C is a factor taking into account the clumpiness of the medium ($C = \langle n_e \rangle^2 / \langle n_e^2 \rangle$), which we assume to be unity. Here we considered the $L_{H\beta}$ to be the luminosity of the GB H β component as measured from our full integrated spectral fit for the quasar and host galaxy, as described in Sect. 2.3.1 and shown in Fig. 2. We note that as in our calculations above, we did not correct for extinction. We performed the equivalent calculation using the GB component of [O III] λ 5007, using the corresponding equation from Carniani et al. (2015):

$$M_{out} = 0.8 \times 10^8 \frac{C}{10^{[O/H]-[O/H]_{\odot}}} \left(\frac{L_{[OIII]}}{10^{44} \text{ erg s}^{-1}} \right) \left(\frac{\langle n_e \rangle}{500 \text{ cm}^{-3}} \right)^{-1} M_{\odot}, \quad (12)$$

and assuming a solar oxygen abundance $[O/H] = [O/H]_{\odot}$. These luminosities and calculated outflow masses are given in

Table 6. By using the luminosities of the outflow component of H β we inferred outflow masses of ionised gas of $(17^{+13}_{-11}) \times 10^7 M_{\odot}$ and $(97^{+14}_{-17}) \times 10^7 M_{\odot}$ for DELS J0411–0907 and VDES J0020–3653, respectively. We note that the masses using the broad, blueshifted component of [O III] λ 5007 are lower than the H β masses, by a factor of approximately two for DELS J0411–0907 and an order of magnitude for VDES J0020–3653. This is a well known issue and it is understood to be a consequence of the ionisation structure of the clouds in the NLR of AGNs, whereby the [O III] λ 5007 only traces a small part of the mass of each cloud (e.g. Perna et al. 2015).

Once the outflow mass is inferred, the ionised outflow rate can be calculated under the thin shell approximation (which generally provides a better description of galactic outflow rates, relative to the uniformly filled outflows, as discussed in Lutz et al. 2020) by using the equation

$$\dot{M}_{out} = \frac{M_{out} v_{out}}{R_{out}} \quad (13)$$

where R_{out} is size of the outflow and v_{out} is its velocity. To estimate R_{out} , we measured the maximum extent from the quasar centre of the [O III] λ 5007 emission with $w_{80} > 600$ km s $^{-1}$, in the BLR-subtracted cube. This $w_{80} > 600$ km s $^{-1}$ is a conservative criterion that has been used in previous studies to classify outflows (e.g. Harrison et al. 2015; Kakkad et al. 2020). We note that for DELS J0411–0907 this outflow region extends from the host galaxy in Region 2 into Region 3, which is seen to have an outflow GB component in Fig. 5. For VDES J0020–3653, when we measured the maximum extent we excluded the south-south-west direction, avoiding the nearby Region 1 which may be artificially contributing to the large w_{80} values as its velocity is offset from the quasar. This R_{out} is a projected radius and it reproduces the true radius only if the directions of the outflow expansion include the plane of the sky. For the outflow velocity we adopted the same approach as Fluetsch et al. (2019) by defining $v_{out} = v_{peak} + v_{FWHM}/2$, where v_{peak} is the peak velocity of the GB component of [O III] λ 5007 (and equivalently H β as they are kinematically tied in our spectral fits) and v_{FWHM} its FWHM. These velocities are measured from our full integrated spectral fit for the quasar and host galaxy, which are given in Table 1. Our measured R_{out} and v_{out} are given in Table 6. Based on these measured values we obtain ionised outflow rates from H β of $58^{+44}_{-37} M_{\odot} \text{ yr}^{-1}$ and $525^{+75}_{-92} M_{\odot} \text{ yr}^{-1}$ for DELS J0411–0907 and VDES J0020–3653, respectively; the [O III] λ 5007 rates are also quoted in Table 6.

We can also estimate the kinetic power of the outflows as

$$P_{K,out} = \frac{1}{2} \dot{M}_{out} v_{out}^2. \quad (14)$$

From the H β outflow, we obtain values of $(3.1^{+2.3}_{-2.0}) \times 10^{43}$ erg s $^{-1}$ and $(51 \pm 9) \times 10^{43}$ erg s $^{-1}$ for DELS J0411–0907 and VDES J0020–3653, respectively, as given in Table 6.

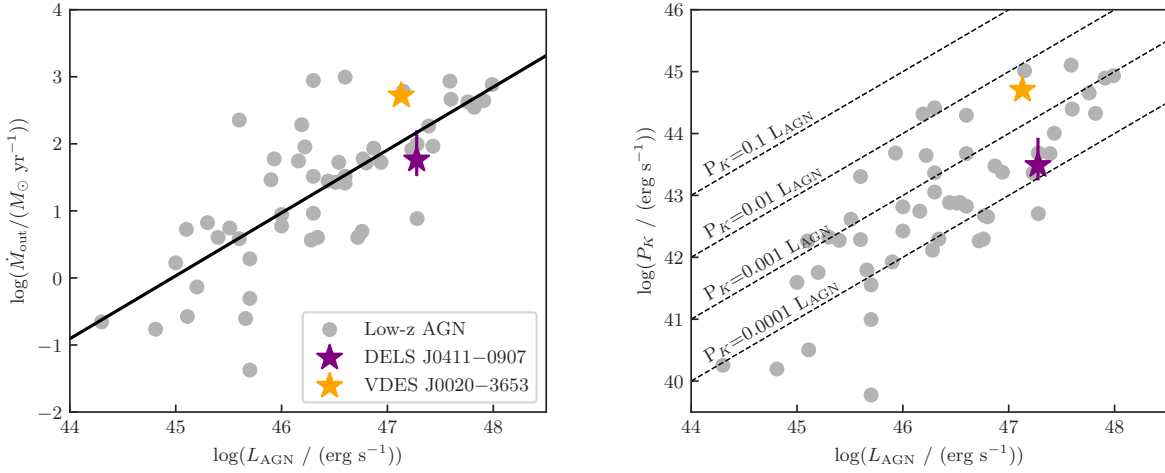


Fig. 10. Outflows of DELS J0411–0907 and VDES J0020–3653. Left: ionised gas outflow mass rate as a function of AGN luminosity, for the two quasars at $z \sim 6.8$ presented in this paper, and for various other AGN at lower redshift ($0 < z < 3$; from [Fiore et al. 2017](#)). The solid line is a linear fit (in logarithmic scales) of the latter data. The ionised outflows of the two quasars at $z \sim 7$ follow the same relation as quasars at lower redshifts. Right: kinetic power (P_K) of the ionised outflows as a function of AGN luminosity (same symbols as in the left plot). The dashed lines show constant ratios of P_K and L_{AGN} as labelled. We note that the [Fiore et al. \(2017\)](#) galaxies have been shifted by $\log(5/2)$ for consistency with our density assumption of 500 cm^{-3} , as they assume 200 cm^{-3} .

The implications of these findings are discussed in Sect. 4.2.

4. Discussion

4.1. Quasar companions

Both of our quasars show additional emission-line regions nearby their host galaxies, which are consistent with being companion galaxies.

For DELS J0411–0907, Region 1 to the south-east of the quasar has a projected offset of $\approx 4.3 \text{ kpc}$ from the quasar, with a widest extent of $\approx 8.8 \text{ kpc}$. From the integrated spectrum we found that this region has a velocity offset relative to the quasar host of $-98 \pm 72 \text{ km s}^{-1}$, indicating minimal line-of-sight offset (Fig. 5 and Table 3). From the emission maps in Figs. 4 and B.1 we see that the velocity spans about 100 km s^{-1} either side of the host velocity. This companion galaxy is likely undergoing a merger with the quasar host. Region 3 exhibits some broader $[\text{O III}] \lambda\lambda 4959, 5007$ emission, indicating an ionised gas outflow in this region, and is likely a tidal tail.

For VDES J0020–3653, Region 1 to the south-south-west of the quasar has a projected offset of $\approx 2.8 \text{ kpc}$ from the quasar, with a widest extent of $\approx 3.6 \text{ kpc}$. This region has a line-of-sight velocity offset by $-55 \pm 72 \text{ km s}^{-1}$ from the host (Figs. 6 and B.1). Region 3 to the north-west of VDES J0020–3653 has a projected offset of $\approx 4.2 \text{ kpc}$ from the quasar, with a widest extent of $\approx 4.6 \text{ kpc}$. This region has a line-of-sight velocity offset by $+83 \pm 72 \text{ km s}^{-1}$ from the host, with the bulk of the gas at a similar offset. Region 4 to the south-west of the quasar has a projected offset of $\approx 5.6 \text{ kpc}$, and a widest extent of $\approx 4.8 \text{ kpc}$. This region has a line-of-sight velocity offset by $+218 \pm 72 \text{ km s}^{-1}$ from the host, again with the bulk of this gas at a similar velocity.

All of these regions satisfy the common merger condition of having a projected distance of $< 20 h^{-1} \text{ kpc}$, where h is the dimensionless Hubble constant $h = H_0 / (100 \text{ km s}^{-1} \text{ Mpc}^{-1})$, and a velocity difference $\delta V < 500 \text{ km s}^{-1}$ (e.g. [Patton et al. 2000](#); [Ceselice et al. 2009](#)).

The presence of quasar companions, or lack thereof, provides important insights into quasar growth mechanisms. For

example, theory predicts that kpc-scale interactions trigger AGN activity (e.g. [Sanders et al. 1988](#); [Hopkins et al. 2006](#)), however mergers and companion galaxies are not ubiquitously observed around low- z quasars ([Cisternas et al. 2011](#); [Kocevski et al. 2012](#); [Mechtley et al. 2016](#); [Marian et al. 2019](#)). However, these early quasars have more intense accretion, and higher merger rates are likely in the early Universe, suggesting that these mergers could be a key driver of this early black hole growth. ALMA observations have detected companion galaxies around high- z quasars at $\approx 8\text{--}60 \text{ kpc}$ separations which are interpreted as major galaxy interactions (e.g. [Wagg et al. 2012](#); [Decarli et al. 2017](#)), at rates of up to 50% in some samples ([Trakhtenbrot et al. 2017](#); [Nguyen et al. 2020](#)). These companions are less frequently observed in the rest-frame UV ([Willott et al. 2005](#)), although some potential companions have been discovered with HST ([McGreer et al. 2014](#); [Marshall et al. 2020](#)). The lack of UV-discovered companions may be due to dust obscuration ([Trakhtenbrot et al. 2017](#)), however our observations which reveal such close neighbours may indicate that resolution has previously limited our ability to identify merging quasars in the early Universe. It is indeed striking that both of our quasars have these companion galaxies, and it will be insightful to see whether other upcoming JWST observations also reveal similar structures around other high- z quasars, building up a larger statistical sample. Discovering these close companions highlights the ability of JWST to understand these early quasars in significantly greater detail, through detailed measurements of their environments and thus potential quasar triggering mechanisms (see also [Perna et al. 2023](#)).

4.2. Quasar driven outflows

In Fig. 10 we show the ionised outflow rate as a function of AGN luminosity for our two quasars at $z \sim 6.8$, and for AGN whose ionised outflows had been measured at lower redshift (from the compilation of [Fiore et al. 2017](#)). Clearly, our two high- z quasars follow the same relation as lower redshift quasars.

The inferred outflow rates ($\sim 58 M_\odot \text{ yr}^{-1}$ for DELS J0411–0907 and $\sim 525 M_\odot \text{ yr}^{-1}$ for VDES J0020–3653) are significantly larger than the upper limits we have measured for the host

SFRs ($<33 M_{\odot} \text{ yr}^{-1}$ for DELS J0411–0907 and $<54 M_{\odot} \text{ yr}^{-1}$ for VDES J0020–3653; see Sect. 3.2.2). These outflow rates are much larger than the SFRs, especially if we consider that the measured outflow rates are only for the ionised component and that the other phases, in particular the molecular phase, may also contribute. This result implies that, if prolonged, the quasar-driven outflow may be the main agent responsible for depleting the galaxy of its gas content. However, one has to take into account that the quasar activity is likely short lived and bursty, hence it may not continue for a time long enough to compete with star formation in depleting the gas mass.

More quantitative consideration on the potential feedback effect of the quasar driven outflow can be obtained by considering the kinetic power of the outflows. Efficient feedback, with high coupling with the ISM, in many scenarios requires that the kinetic power of the outflow should be about 5–7% of the AGN bolometric luminosity. The right panel of Fig. 10 shows the kinetic power of ionised outflows as a function of AGN luminosity, where locii of constant P_K/L_{AGN} ratio are also indicated with dashed lines. Clearly, the ionised outflows of two quasars at $z \sim 6.8$ have a kinetic power that is less than 1% of L_{AGN} (in the case of DELS J0411–0907 actually $<0.1\%$), indicating that the outflow may not be an effective feedback mechanism.

Moreover, the momentum rate ($\dot{M}_{\text{out}} v_{\text{out}}$) of the two quasars is $0.07 L_{\text{AGN}}/c$ and $1.28 L_{\text{AGN}}/c$ for DELS J0411–0907 and VDES J0020–3653, respectively. These values are much lower than expected by the (very feedback-effective) energy-driven outflows, which expect a momentum boost by a factor of ~ 20 relative to the radiation momentum rate L_{AGN}/c . Based on these values, these outflows seem to be more consistent with momentum-driven outflows, possibly resulting from radiation pressure on the dusty clouds (Fabian 2012; Costa et al. 2014). However, once again, we caution that with our NIRSpect data we can only probe the ionised phase of these outflows. The other phases of the outflows, and in particular the molecular component, may be much more massive and energetic (Fluetsch et al. 2019), although Fiore et al. (2017) suggest that at such high luminosities the ionised outflows may be comparable or stronger than the other phases. Future deep observations with ALMA may provide constraints on the other phases of these outflows and, therefore, provide additional information on the feedback role of AGN-driven outflows in these two early quasars.

5. Conclusions

We have analysed JWST NIRSpect IFU observations of two $z \approx 6.8$ quasars, DELS J0411–0907 and VDES J0020–3653. By analysing their integrated quasar spectrum, we measured black hole masses from the $H\beta$ and $H\alpha$ broad lines, which are the most reliable single-epoch mass estimators. These are some of the first observations of Balmer broad emission lines in high- z quasars, making such a measurement possible for the first time. We derived a best estimate for the black hole mass in DELS J0411–0907 of $M_{\text{BH}} = 1.85^{+2}_{-0.8} \times 10^9 M_{\odot}$, implying an Eddington ratio of $\lambda_{\text{Edd}} = 0.8^{+0.7}_{-0.4}$. This is more massive than the Mg II mass estimates of $M_{\text{BH,MgII}} = (0.6-1) \times 10^9 M_{\odot}$ which implied more extreme Eddington ratios of $\lambda_{\text{Edd}} = 1.3-2.4$. By measuring a more accurate black hole mass, we have revised our understanding of the accretion physics of this early quasar. For VDES J0020–3653, our best estimate of the black hole mass is $M_{\text{BH}} = 2.9^{+3.5}_{-1.3} \times 10^9 M_{\odot}$, corresponding to an Eddington ratio of $\lambda_{\text{Edd}} = 0.4^{+0.3}_{-0.2}$. This is more consistent with the Mg II measurements of Reed et al. (2019). Together, these quasars show that

the Mg II black hole mass can be significantly biased relative to the $H\beta$ estimate for some high- z quasars, while for others these two techniques may give consistent black hole mass measurements, highlighting the benefit of measuring these more reliable $H\beta$ masses.

We performed quasar subtraction on our IFU observations, by modelling the PSF using the variation in the flux of the quasar broad $H\alpha$ and $H\beta$ lines across the spatial domain. From this subtraction, we revealed that the host galaxy of DELS J0411–0907 shows emission extending to a radius of 2.5 kpc, described by a 2D Gaussian with semi-major axis $\sigma = 0.75$ kpc. This host has narrow [O III] $\lambda\lambda 4959, 5007$, $H\beta$, and $H\alpha$ emission, alongside a broader wing emission from an outflow. We estimated that the host has a SFR of $<33 M_{\odot} \text{ yr}^{-1}$, with a dynamical mass in the range of $2.6-16 \times 10^{10} M_{\odot}$ with a best estimate of $8.6^{+4.4}_{-3.3} \times 10^{10} M_{\odot}$. This host galaxy lies within the AGN-dominated regime of the low- z BPT diagram.

The host galaxy of VDES J0020–3653 has emission extending to a radius of 2.1 kpc, described by a 2D Gaussian with semi-major axis $\sigma = 1.0$ kpc. Both narrow [O III] $\lambda\lambda 4959, 5007$, $H\beta$, and $H\alpha$ and broad-wing emission is detected. We estimated a SFR of $<54 M_{\odot} \text{ yr}^{-1}$ for this host, with a dynamical mass between $4.6-17 \times 10^{10} M_{\odot}$ with a best estimate of $17^{+18}_{-8} \times 10^{10} M_{\odot}$. The host of VDES J0020–3653 lies within the star-forming or transition region of the low- z BPT diagram; however, this is likely due to the low metallicity of these quasar hosts, with low-metallicity, high- z AGN predicted to lie in this region.

We found that from our measured black hole and dynamical masses, DELS J0411–0907 and VDES J0020–3653 both lie slightly above the local black hole–host mass relation (Kormendy & Ho 2013) and are consistent with the existing observations of $z \gtrsim 6$ quasar host galaxies with ALMA. Both quasars are found to have additional emission-line regions near their host galaxies, with two regions for DELS J0411–0907 and three for VDES J0020–3653. We have studied these companion regions, measuring their SFRs, excitation mechanisms, and kinematics. We found that four companion regions are likely to be either galaxies merging with the quasar host galaxy, and one an extended tidal tail. It is striking that both of our high- z quasars are undergoing galaxy mergers, and it will be insightful to see the fraction of high- z quasars that are found to also have companions in future NIRSpect IFU observations.

We detect ionised outflows in [O III] $\lambda\lambda 4959, 5007$, and $H\beta$ from both VDES J0020–3653 and DELS J0411–0907. We measured the rates of the ionised outflow from $H\beta$ to be $58^{+44}_{-37} M_{\odot} \text{ yr}^{-1}$ for DELS J0411–0907 and $525^{+75}_{-92} M_{\odot} \text{ yr}^{-1}$ for VDES J0020–3653. These outflow rates are much larger than the SFRs of the host galaxies, implying that if this is prolonged, the quasar-driven outflow may be the main driver for gas depletion within the galaxies. We found that these outflows are likely momentum-driven, and are not likely to be effective feedback mechanisms.

This work highlights the exquisite capabilities of the JWST NIRSpect IFU for observing high- z quasars. With the high-resolution spectral coverage in the infrared, we are able to study key rest-frame optical emission lines that have been previously unobservable, such as $H\beta$, [O III] $\lambda\lambda 4959, 5007$, and $H\alpha$. This has allowed us to measure the black hole masses and Eddington ratios of these quasars more accurately than had been previously possible. Obtaining spatially resolved IFU spectra has also allowed us to study the host galaxies, local environments, and outflow properties of these quasars in great detail. Overall, this work shows the possibilities of the NIRSpect IFU, and we look forward to the insights that this instrument will give about the

formation and growth of quasars and their host galaxies in the early Universe.

Acknowledgements. We thank the anonymous referee for their constructive feedback which greatly improved the manuscript. We thank Bernd Husemann for his help with the QDeblend3D software and sharing his expertise on quasar subtraction. M.M. would like to thank Toby Brown for his helpful advice, particularly on creating the kinematic maps. This work is based on observations made with the NASA/ESA/CSA *James Webb* Space Telescope. The data were obtained from the Mikulski Archive for Space Telescopes at the Space Telescope Science Institute, which is operated by the Association of Universities for Research in Astronomy, Inc., under NASA contract NAS 5-03127 for JWST. These observations are associated with programme #1222, as part of the Galaxy Assembly with NIRSpec IFS GTO programme. M.A.M. acknowledges the support of a National Research Council of Canada Plaskett Fellowship, and the Australian Research Council Centre of Excellence for All Sky Astrophysics in 3 Dimensions (ASTRO 3D), through project number CE170100013. S.A., B.R.P. and M.P. acknowledge support from the research project PID2021-127718NB-I00 of the Spanish Ministry of Science and Innovation/State Agency of Research (MICIN/AEI). M.P. also acknowledges support from the Programa Atracción de Talento de la Comunidad de Madrid via grant 2018-T2/TIC-11715. R.M., J.S. and F.D.E. acknowledge support by the Science and Technology Facilities Council (STFC), from the ERC Advanced Grant 695671 ‘QUENCH’. R.M. and J.S. also acknowledge funding from a research professorship from the Royal Society. G.C. acknowledges the support of the INAF Large Grant 2022 ‘The metal circle: a new sharp view of the baryon cycle up to Cosmic Dawn with the latest generation IFU facilities’. H.Ü. gratefully acknowledges support by the Isaac Newton Trust and by the Kavli Foundation through a Newton-Kavli Junior Fellowship. A.J.B., G.C.J. and A.J.C. acknowledge funding from the ‘FirstGalaxies’ Advanced Grant from the European Research Council (ERC) under the European Union’s Horizon 2020 research and innovation programme (Grant agreement No. 789056). S.C. acknowledges support from the European Union (ERC, WINGS, 101040227). P.G.P.-G. acknowledges support from Spanish Ministerio de Ciencia e Innovación MCIN/AEI/10.13039/501100011033 through grant PGC2018-093499-B-I00. The Cosmic Dawn Center (DAWN) is funded by the Danish National Research Foundation under grant no. 140. This research has made use of NASA’s Astrophysics Data System, QFitsView, and SAOImageDS9, developed by Smithsonian Astrophysical Observatory. This paper made use of Python packages and software AstroPy (Astropy Collaboration 2013), Matplotlib (Hunter 2007), NumPy (van der Walt et al. 2011), Pandas (Pandas Development Team 2020), Photutils (Bradley et al. 2018), Regions (Bradley et al. 2022), SciPy (Virtanen et al. 2020), Seaborn (Waskom 2021), Spectral Cube (Ginsburg et al. 2019), QDeblend3D (Husemann et al. 2013, 2014), and QubeSpec (<https://github.com/honzascholtz/Qubespec>).

References

- Abazajian, K. N., Adelman-McCarthy, J. K., Agüeros, M. A., et al. 2009, *ApJS*, **182**, 543
- Astropy Collaboration (Robitaille, T. P., et al.) 2013, *A&A*, **558**, A33
- Baldwin, J. A., Phillips, M. M., & Terlevich, R. 1981, *PASP*, **93**, 5
- Banados, E., Schindler, J.-T., Venemans, B. P., et al. 2022, *ApJS*, **265**, 29
- Bañados, E., Venemans, B. P., Decarli, R., et al. 2016, *ApJS*, **227**, 11
- Bañados, E., Venemans, B. P., Mazzucchelli, C., et al. 2018, *Nature*, **553**, 473
- Bertoldi, F., Cox, P., Neri, R., et al. 2003, *A&A*, **409**, L47
- Bischetti, M., Feruglio, C., D’Odorico, V., et al. 2022, *Nature*, **605**, 244
- Bischetti, M., Fiore, F., Feruglio, C., et al. 2023, *ApJ*, **952**, 44
- Böker, T., Arribas, S., Lützgendorf, N., et al. 2022, *A&A*, **661**, A82
- Böker, T., Beck, T. L., Birkmann, S. M., et al. 2023, *PASP*, **135**, 038001
- Bradley, L., Sipocz, B., Robitaille, T., et al. 2018, <https://doi.org/10.5281/zenodo.1340699>
- Bradley, L., Deil, C., Ginsburg, A., et al. 2022, <https://doi.org/10.5281/zenodo.7259631>
- Bruzual, G., & Charlot, S. 2003, *MNRAS*, **344**, 1000
- Bushouse, H., Eisenhamer, J., Dencheva, N., et al. 2022, <https://doi.org/10.5281/zenodo.7229890>
- Calzetti, D., Armus, L., Bohlin, R. C., et al. 2000, *ApJ*, **533**, 682
- Cappellari, M., Bacon, R., Bureau, M., et al. 2006, *MNRAS*, **366**, 1126
- Carniani, S., Marconi, A., Maiolino, R., et al. 2015, *A&A*, **580**, A102
- Cisternas, M., Jahnke, K., Inskip, K. J., et al. 2011, *ApJ*, **726**, 57
- Coatman, L., Hewett, P. C., Banerji, M., & Richards, G. T. 2016, *MNRAS*, **461**, 647
- Conselice, C. J., Yang, C., & Bluck, A. F. L. 2009, *MNRAS*, **394**, 1956
- Costa, T., Sijacki, D., & Haehnelt, M. G. 2014, *MNRAS*, **444**, 2355
- Cresci, G., Mainieri, V., Brusa, M., et al. 2015, *ApJ*, **799**, 82
- Decarli, R., Walter, F., Yang, Y., et al. 2012, *ApJ*, **756**, 150
- Decarli, R., Walter, F., Venemans, B. P., et al. 2017, *Nature*, **545**, 457
- Decarli, R., Walter, F., Venemans, B. P., et al. 2018, *ApJ*, **854**, 97
- Ding, X., Onoue, M., Silverman, J. D., et al. 2023, *Nature*, **621**, 51
- Domínguez, A., Siana, B., Henry, A. L., et al. 2013, *ApJ*, **763**, 145
- Dunlop, J. S., McLure, R. J., Kulkula, M. J., et al. 2003, *MNRAS*, **340**, 1095
- Eilers, A.-C., Simcoe, R. A., Yue, M., et al. 2022, *ApJ*, **950**, 68
- Fabian, A. 2012, *ARA&A*, **50**, 455
- Fan, X., White, R. L., Davis, M., et al. 2000, *AJ*, **120**, 1167
- Fan, X., Narayanan, V. K., Lupton, R. H., et al. 2001, *AJ*, **122**, 2833
- Fan, X., Strauss, M. A., Schneider, D. P., et al. 2003, *AJ*, **125**, 1649
- Farina, E. P., Schindler, J.-T., Walter, F., et al. 2022, *ApJ*, **941**, 106
- Feltre, A., Charlot, S., & Gutkin, J. 2016, *MNRAS*, **456**, 3354
- Fiore, F., Feruglio, C., Shankar, F., et al. 2017, *A&A*, **601**, A143
- Fluetsch, A., Maiolino, R., Carniani, S., et al. 2019, *MNRAS*, **483**, 4586
- Gardner, J. P., Mather, J. C., Clampin, M., et al. 2006, *Space Sci. Rev.*, **123**, 485
- Gardner, J. P., Mather, J. C., Abbott, R., & Zondag, E. 2023, *PASP*, **135**, 068001
- Ginolfi, M., Maiolino, R., Carniani, S., et al. 2018, *MNRAS*, **476**, 2421
- Ginsburg, A., Koch, E., Robitaille, T., et al. 2019, <https://doi.org/10.5281/zenodo.3558614>
- Greene, J. E., & Ho, L. C. 2005, *ApJ*, **630**, 122
- Harikane, Y., Zhang, Y., Nakajima, K., et al. 2023, ArXiv e-prints [arXiv:2303.11946]
- Harrison, C. M., Alexander, D. M., Mullaney, J. R., et al. 2015, *MNRAS*, **456**, 1195
- Hinshaw, G., Larson, D., Komatsu, E., et al. 2013, *ApJS*, **208**, 19
- Hirschmann, M., Charlot, S., Feltre, A., et al. 2023, *MNRAS*, **526**, 3610
- Hopkins, P. F., Hernquist, L., Cox, T. J., et al. 2006, *ApJS*, **163**, 1
- Hunter, J. D. 2007, *Comput. Sci. Eng.*, **9**, 90
- Husemann, B., Wisotzki, L., Sánchez, S. F., & Jahnke, K. 2013, *A&A*, **549**, A43
- Husemann, B., Jahnke, K., Sánchez, S. F., et al. 2014, *MNRAS*, **443**, 755
- Hutchings, J. B. 2003, *AJ*, **125**, 1053
- Izumi, T., Onoue, M., Shirakata, H., et al. 2018, *PASJ*, **70**, 36
- Izumi, T., Onoue, M., Matsuoka, Y., et al. 2019, *PASJ*, **71**, 111
- Jakobsen, P., Ferruit, P., de Oliveira, C. A., et al. 2022, *A&A*, **661**, A80
- Kakkad, D., Mainieri, V., Vietri, G., et al. 2020, *A&A*, **642**, A147
- Kashikawa, N., Ishizaki, Y., Willott, C. J., et al. 2015, *ApJ*, **798**, 28
- Kashino, D., Lilly, S. J., Matthee, J., et al. 2022, *ApJ*, **950**, 66
- Kaspi, S., Smith, P. S., Netzer, H., et al. 2000, *ApJ*, **533**, 631
- Kaspi, S., Brandt, W. N., Maoz, D., et al. 2021, *ApJ*, **915**, 129
- Kaufmann, G., Heckman, T. M., Tremonti, C., et al. 2003, *MNRAS*, **346**, 1055
- Kennicutt, R. C. 1998, *ARA&A*, **36**, 189
- Kennicutt, R. C., & Evans, N. J. 2012, *ARA&A*, **50**, 531
- Kewley, L. J., Dopita, M. A., Sutherland, R. S., Heisler, C. A., & Trevena, J. 2001, *ApJ*, **556**, 121
- Kocevski, D. D., Faber, S. M., Mozena, M., et al. 2012, *ApJ*, **744**, 148
- Kormendy, J., & Ho, L. C. 2013, *ARA&A*, **51**, 511
- Kovacevic, J., Popovic, L. C., & Dimitrijevic, M. S. 2010, *ApJS*, **189**, 15
- Kuraszkiewicz, J. K., Green, P. J., Forster, K., et al. 2002, *ApJS*, **143**, 257
- Law, D. D., Morrison, J. E., Argyriou, I., et al. 2023, *AJ*, **166**, 45
- Lee, J. C., de Paz, A. G., Tremonti, C., et al. 2009, *ApJ*, **706**, 599
- Lutz, D., Sturm, E., Janssen, A., et al. 2020, *A&A*, **633**, A134
- Marian, V., Jahnke, K., Mechtley, M., et al. 2019, *ApJ*, **882**, 141
- Marshall, M. A., Mechtley, M., Windhorst, R. A., et al. 2020, *ApJ*, **900**, 21
- Marshall, M. A., Wyithe, J. S. B., Windhorst, R. A., et al. 2021, *MNRAS*, **506**, 1209
- Matsuoka, Y., Onoue, M., Kashikawa, N., et al. 2018, *PASJ*, **70**, S10
- McElwain, M. W., Feinberg, L. D., Perrin, M. D., et al. 2023, *PASP*, **135**, 058001
- McGreer, I. D., Fan, X., Strauss, M. A., et al. 2014, *AJ*, **148**, 73
- McLeod, K. K., & Rieke, G. H. 1994, *ApJ*, **420**, 58
- Mechtley, M., Windhorst, R. A., Ryan, R. E., et al. 2012, *ApJ*, **756**, L38
- Mechtley, M., Jahnke, K., Windhorst, R. A., et al. 2016, *ApJ*, **830**, 156
- Nagao, T., Marconi, A., & Maiolino, R. 2006, *A&A*, **447**, 157
- Nakajima, K., & Maiolino, R. 2022, *MNRAS*, **513**, 5134
- Neelaman, M., Novak, M., Venemans, B. P., et al. 2021, *ApJ*, **911**, 141
- Nguyen, N. H., Lira, P., Trakhtenbrot, B., et al. 2020, *ApJ*, **895**, 74
- Onoue, M., Kashikawa, N., Matsuoka, Y., et al. 2019, *ApJ*, **880**, 77
- Osterbrock, D. E. 1989, *Astrophysics of Gaseous Nebulae and Active Galactic Nuclei* (Mill Valley: University Science Books)
- Pandas Development Team 2020, <https://doi.org/10.5281/zenodo.3509134>
- Patton, D. R., Carlberg, R. G., Marzke, R. O., et al. 2000, *ApJ*, **536**, 153
- Pensabene, A., Carniani, S., Perna, M., et al. 2020, *A&A*, **637**, A84
- Perna, M., Brusa, M., Cresci, G., et al. 2015, *A&A*, **574**, A82
- Perna, M., Arribas, S., Marshall, M., et al. 2023, *A&A*, accepted [arXiv:2304.06756]
- Peterson, B. M. 2009, *Proc. Int. Astron. Union*, **5**, 151

- Pons, E., McMahon, R. G., Simcoe, R. A., et al. 2019, *MNRAS*, 484, 5142
- Rankine, A. L., Hewett, P. C., Banerji, M., & Richards, G. T. 2020, *MNRAS*, 492, 4553
- Reed, S. L., Banerji, M., Becker, G. D., et al. 2019, *MNRAS*, 487, 1874
- Riechers, D. A., Walter, F., Carilli, C. L., & Bertoldi, F. 2007, *ApJ*, 671, L13
- Rigby, J., Perrin, M., McElwain, M., et al. 2022, *PASP*, 135, 048001
- Sanders, D. B., Soifer, B. T., Elias, J. H., et al. 1988, *ApJ*, 325, 74
- Schmidt, M. 1963, *Nature*, 197, 1040
- Shen, Y., & Kelly, B. C. 2012, *ApJ*, 746, 169
- Shen, Y., Greene, J. E., Strauss, M. A., Richards, G. T., & Schneider, D. P. 2008, *ApJ*, 680, 169
- Shen, Y., Richards, G. T., Strauss, M. A., et al. 2011, *ApJS*, 194, 45
- Sijacki, D., Springel, V., & Haehnelt, M. G. 2009, *MNRAS*, 400, 100
- Strom, A. L., Steidel, C. C., Rudie, G. C., et al. 2017, *ApJ*, 836, 164
- Sun, J. 2020, *Sun_Astro_Tools*, [GitHub](#)
- Sun, J., Leroy, A. K., Schrubba, A., et al. 2018, *ApJ*, 860, 172
- Trakhtenbrot, B., Lira, P., Netzer, H., et al. 2017, *ApJ*, 836, 8
- Trevese, D., Perna, M., Vagnetti, F., Saturni, F. G., & Dadina, M. 2014, *ApJ*, 795, 164
- Übler, H., Maiolino, R., Curtis-Lake, E., et al. 2023, *A&A*, 677, A145
- van der Walt, S., Colbert, S. C., & Varoquaux, G. 2011, *Comput. Sci. Eng.*, 13, 22
- van der Wel, A., van Houdt, J., Bezanson, R., et al. 2022, *ApJ*, 936, 9
- van Dokkum, P. G. 2001, *PASP*, 113, 1420
- Vayner, A., Wright, S. A., Do, T., et al. 2016, *ApJ*, 821, 64
- Veilleux, S., & Osterbrock, D. E. 1987, *ApJS*, 63, 295
- Venemans, B. P., Walter, F., Zschaechner, L., et al. 2015, *ApJ*, 816, 37
- Venemans, B. P., Walter, F., Decarli, R., et al. 2017, *ApJ*, 837, 146
- Vestergaard, M., & Osmer, P. S. 2009, *ApJ*, 699, 800
- Vestergaard, M., & Peterson, B. M. 2006, *ApJ*, 641, 689
- Virtanen, P., Gommers, R., Oliphant, T. E., et al. 2020, *Nat. Meth.*, 17, 261
- Volonteri, M., & Rees, M. J. 2005, *ApJ*, 633, 624
- Volonteri, M., Silk, J., & Dubus, G. 2015, *ApJ*, 804, 148
- Wagg, J., Wiklind, T., Carilli, C. L., et al. 2012, *ApJ*, 752, L30
- Walter, F., Bertoldi, F., Carilli, C., et al. 2003, *Nature*, 424, 406
- Walter, F., Carilli, C., Bertoldi, F., et al. 2004, *ApJ*, 615, L17
- Walter, F., Neeleman, M., Decarli, R., et al. 2022, *ApJ*, 927, 21
- Wandel, A., Peterson, B. M., & Malkan, M. A. 1999, *ApJ*, 526, 579
- Wang, R., Carilli, C. L., Neri, R., et al. 2010, *ApJ*, 714, 699
- Wang, R., Wagg, J., Carilli, C. L., et al. 2011, *AJ*, 142, 101
- Wang, R., Wagg, J., Carilli, C. L., et al. 2013, *ApJ*, 773, 44
- Wang, F., Yang, J., Fan, X., et al. 2018, *ApJ*, 869, L9
- Wang, F., Yang, J., Fan, X., et al. 2019, *ApJ*, 884, 30
- Waskom, M. 2021, *J. Open Source Softw.*, 6, 3021
- Willott, C. J., Percival, W. J., McLure, R. J., et al. 2005, *ApJ*, 626, 657
- Willott, C. J., Delorme, P., Reylé, C., et al. 2009, *AJ*, 137, 3541
- Willott, C. J., Albert, L., Arzoumanian, D., et al. 2010, *AJ*, 140, 546
- Willott, C. J., Bergeron, J., & Omont, A. 2015, *ApJ*, 801, 123
- Willott, C. J., Bergeron, J., & Omont, A. 2017, *ApJ*, 850, 108
- Wisnioski, E., Mendel, J. T., Schreiber, N. M. F., et al. 2018, *ApJ*, 855, 97
- Wu, X.-B., Wang, F., Fan, X., et al. 2015, *Nature*, 518, 512
- Yang, J., Wang, F., Fan, X., et al. 2021, *ApJ*, 923, 262
- Yang, J., Fan, X., Gupta, A., et al. 2023a, AAS, submitted [arXiv:2302.01777]
- Yang, J., Wang, F., Fan, X., et al. 2023b, *ApJ*, 951, L5
- Zakamska, N. L., & Greene, J. E. 2014, *MNRAS*, 442, 784

Appendix A: Measured PSFs

The measured PSFs from the N&B quasar subtraction, for both $H\alpha$ and $H\beta$, are shown for the two quasars in Figure A.1. We note that for VDES J0020–3653 the PSF shape does not follow the typical expected 6-pointed JWST PSF. This data cube is a combination of two separate observations taken at different position angles, 160.169 and 188.177 degrees, and so the resulting PSF

of this combined cube would theoretically be two of the standard 6-point PSFs superimposed, one rotated by 28 degrees.

As the quasar subtraction technique measures the PSF from the data cube itself, and does not rely on PSF models, this does not affect our results. We have performed the quasar subtraction separately on both halves of the observation as a test, and verify that the host and companion features appear in both halves and are not distorted by this combination.

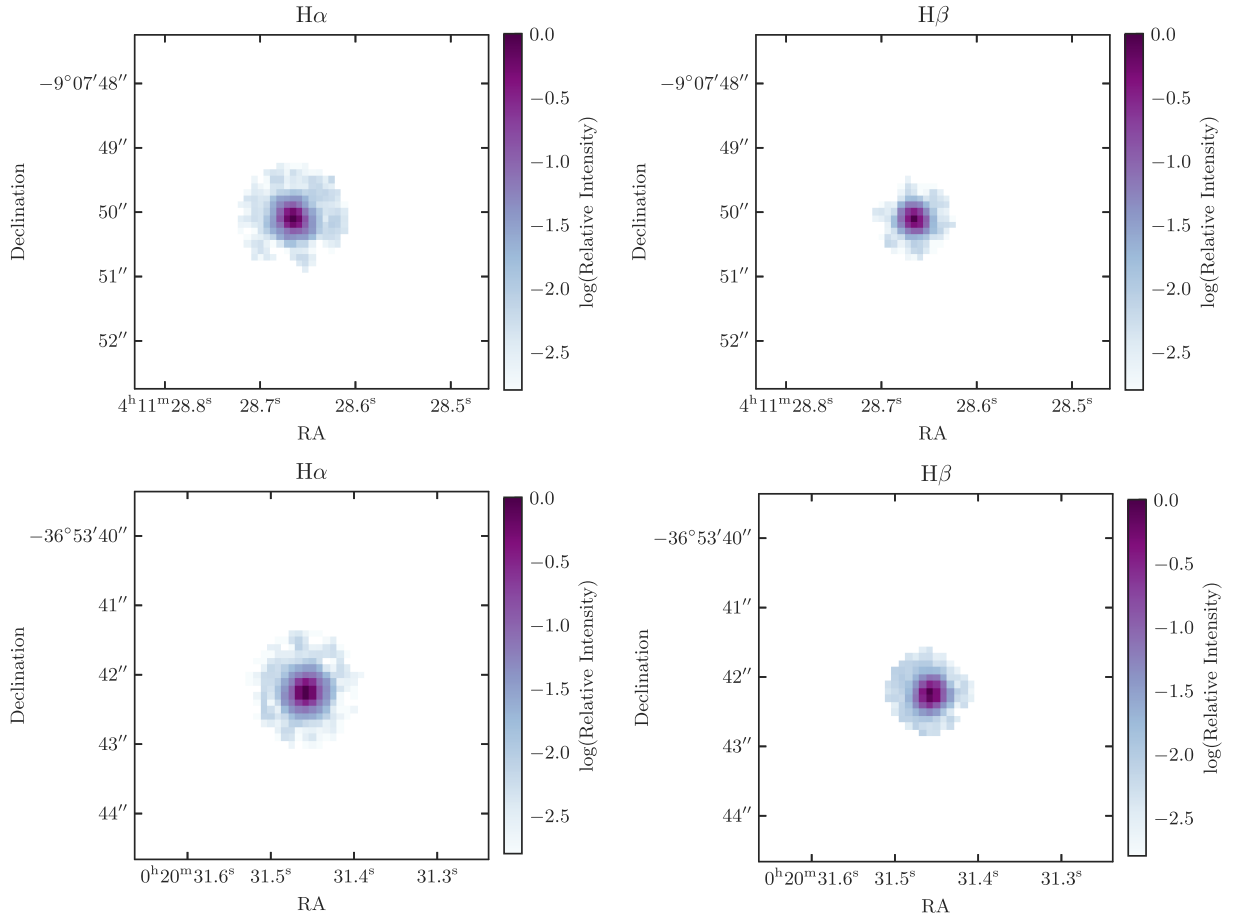


Fig. A.1. PSFs measured from the broad $H\alpha$ and $H\beta$ lines from DELSJ0411–0907 (top) and VDES J0020–3653 (bottom), from the N&B quasar subtraction, as described in Section 2.3.3. These were created from the best fit quasar cube, which is the peak quasar spectrum scaled in flux to match the observed broad line flux in each spaxel. The relative intensity here depicts this scaling factor, which is the amount of flux in each spaxel relative to the brightest spaxel. We created two PSFs for each quasar, one from each of $H\alpha$ and $H\beta$, as the PSF varies with wavelength.

Appendix B: Kinematic maps using the BLR subtraction technique

Our kinematic maps for DELS J0411–0907 and VDES J0020–3653 as measured from the BLR quasar subtracted cubes are

shown in Figure B.1. This can be compared to Figures 4 and Figures 6, which show the equivalent maps for the N&B quasar subtracted cubes for DELS J0411–0907 and VDES J0020–3653 respectively.

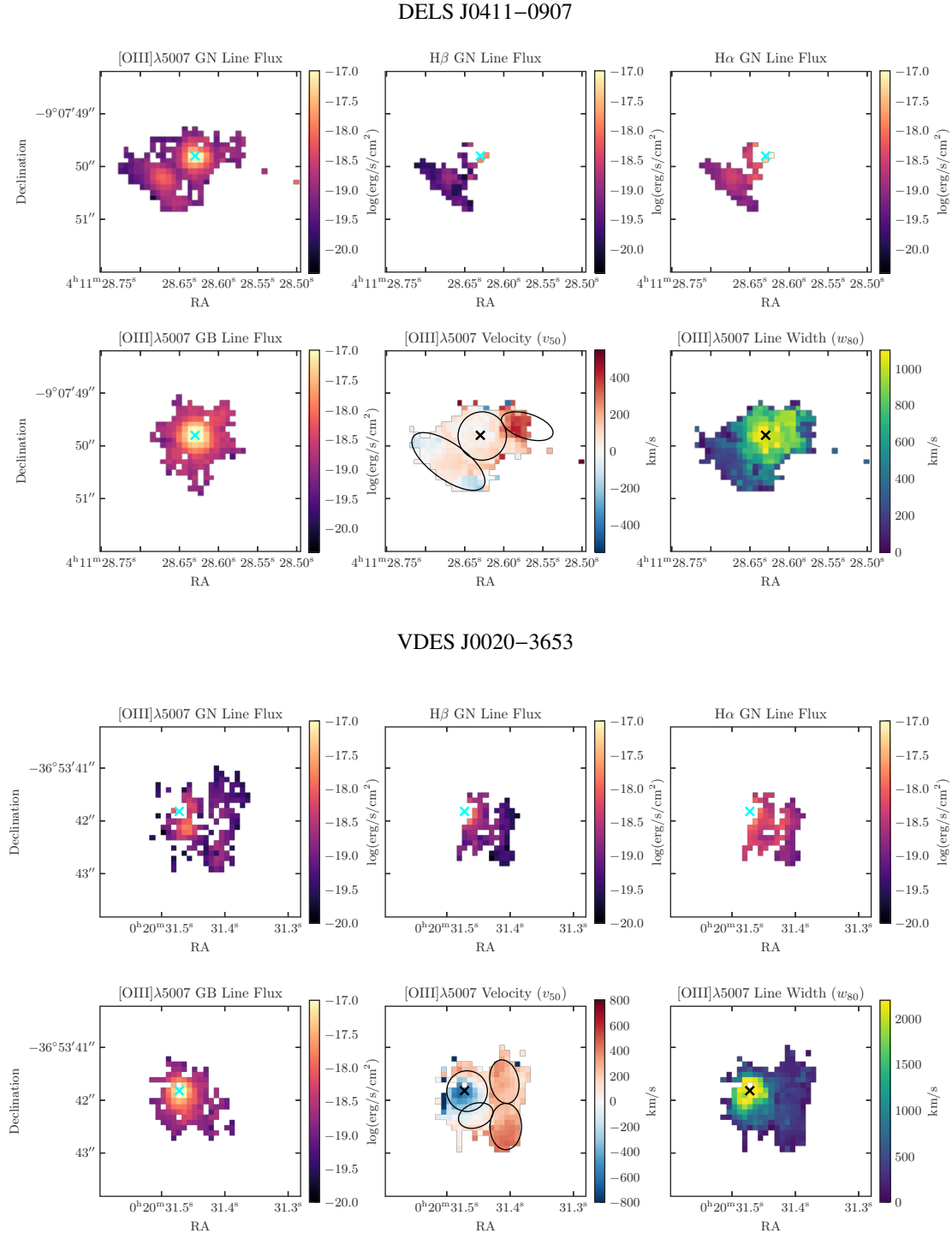


Fig. B.1. Kinematic maps for DELS J0411–0907 (top) and VDES J0020–3653 (bottom), after the subtraction of the quasar emission using the BLR subtraction technique. The top panels show the flux of the narrow component of the [O III] $\lambda 5007$, H β , and H α lines (GN), as fit by a Gaussian. The [O III] $\lambda 4959$ line is not shown as it was constrained to have an amplitude three times fainter than that of [O III] $\lambda 5007$. The bottom left panel shows the flux of the broader GB component of the [O III] $\lambda 5007$ line, a second Gaussian with a larger σ . The lower middle and right panels show our kinematic maps, showing the non-parametric central velocity of the line (v_{50} ; middle) and the line width (w_{80} ; right). As these are non-parametric, this combines both the GN and GB components. We describe our method for creating these maps in Section 2.3.4. The black ellipses in the lower middle panels depict the regions as in Figures 5 and 7.

Appendix C: Data cubes with pixel sub-sampling

Throughout this work we used data cubes with the native spaxel spatial size of $0.1''/\text{pix}$, produced using the EMSM weighting to combine the various dither positions. With our dithering strategy it is also possible to sub-sample the data down to a pixel size of $0.05''/\text{pix}$, to improve the spatial resolution which is limited by the pixel scale. For the best possible spatial resolution, we used cubes with a pixel scale of $0.05''$ that have been combined using the *drizzle* weighting. This weighting optimises the resolution, but is more affected by the PSF effects (see Perna et al. 2023, for details). These $0.05''/\text{pix}$ *drizzle* cubes are highly affected by the PSF oscillations and chromatic effects, which we found result in very poor results for the quasar subtraction. Because the $0.1''/\text{pix}$ pixels optimise the S/N, and, most critically, give significantly improved results for the quasar subtraction that is the focus of our work, we used these $0.1''/\text{pix}$ EMSM cubes throughout this paper.

However, the $0.05''/\text{pix}$ *drizzle* cubes are more optimal for looking at the structural or morphological properties beyond the quasar host galaxy itself. In Figure C.1 we show the [O III] $\lambda 5007$ flux maps for DELS J0411–0907 and VDES J0020–3653 using cubes that have been produced with $0.05''$ pixels, combined using the *drizzle* weighting, following the method described in detail in Perna et al. (2023). This shows the companion galaxy

morphology in greater detail. We found that in general, the morphology is consistent with our results from the $0.1''/\text{pix}$ cubes, showing a companion to the south-east of DELS J0411–0907 with a potential outflow to the north-west, and the two companion regions to the west of VDES J0020–3653.

One key difference is that the higher spatial resolution data for VDES J0020–3653 reveals a second distinct peak in the [O III] $\lambda 5007$ emission, separated by only $\sim 0.37''$ or 2 kpc (quasar peak to companion peak) to the south-south-west of the quasar. This very nearby companion, with a velocity offset by -179 km/s from the host Region 2 (GN), or -30 km/s with respect to the quasar’s peak [O III] $\lambda 5007$ emission at $z = 6.854$, would be significantly interacting with the quasar host galaxy. This is so close to the quasar host that in the $0.1''/\text{pix}$ cubes this appears to be one elongated galaxy. Thus, if this region is not considered separately, and instead one elongated ellipse for this full emission region was chosen, we would overestimate the fluxes of the host galaxy of VDES J0020–3653. To account for this, we used the structure seen in Figure C.1 to define our region ellipses as seen in Figure 7, which we used to extract and thus analyse the individual regions’ spectra.

As we could not perform a reliable quasar subtraction on the higher resolution cubes, we did not use the cubes throughout this work. Our results focus on the host detection and thus require an accurate quasar subtraction.

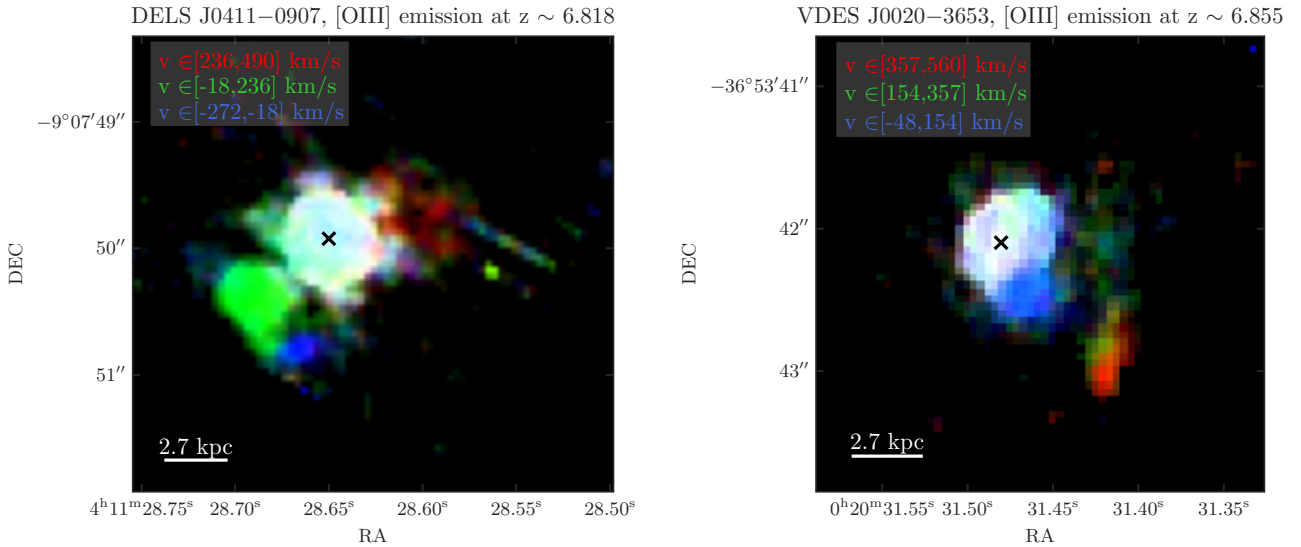


Fig. C.1. [O III] $\lambda 5007$ flux maps for DELS J0411–0907 (left) and VDES J0020–3653 (right) using data cubes that have been produced with $0.05''/\text{pix}$ pixels, combined using the *drizzle* weighting, following the method described in detail in Perna et al. (2023). These maps were made using the original, non-continuum subtracted cubes. The stacked red, green, and blue images depict the integral of the flux across each of the specified wavelength or velocity windows, relative to the quasar redshift. The quasar peak location is marked as a black cross.